RESEARCH ARTICLE SUMMARY

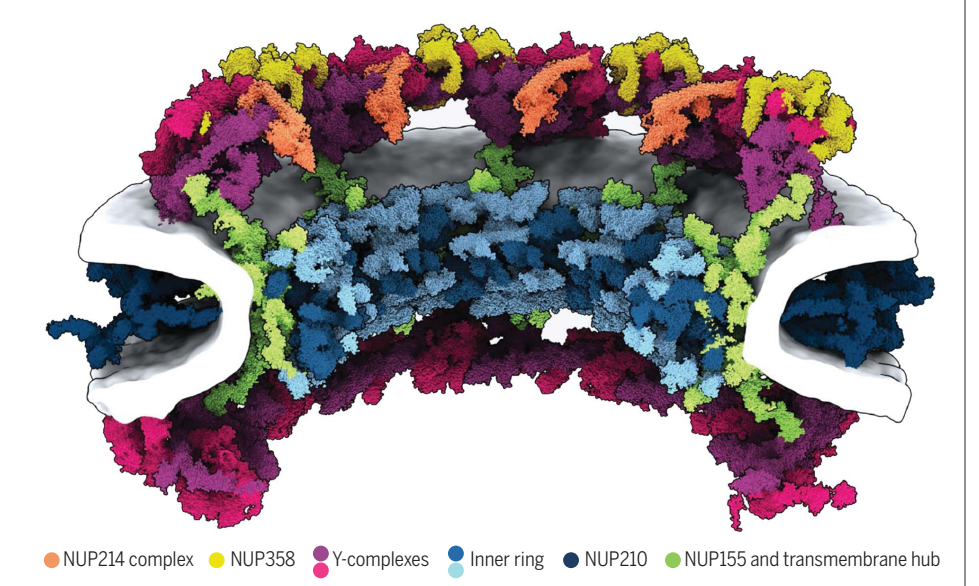
NUCLEAR PORE COMPLEX

Al-based structure prediction empowers integrative structural analysis of human nuclear pores

Shyamal Mosalaganti†, Agnieszka Obarska-Kosinska†, Marc Siggel†, Reiya Taniguchi, Beata Turoňová, Christian E. Zimmerli, Katarzyna Buczak, Florian H. Schmidt, Erica Margiotta, Marie-Therese Mackmull, Wim J. H. Hagen, Gerhard Hummer*, Jan Kosinski*, Martin Beck*

INTRODUCTION: The eukaryotic nucleus protects the genome and is enclosed by the two membranes of the nuclear envelope. Nuclear pore complexes (NPCs) perforate the nuclear envelope to facilitate nucleocytoplasmic transport. With a molecular weight of ~120 MDa, the human NPC is one of the largest protein complexes. Its ~1000 proteins are taken in multiple copies from a set of about 30 distinct nucleoporins (NUPs). They can be roughly categorized into two classes. Scaffold NUPs contain folded domains and form a cylindrical scaffold architecture around a central channel. Intrinsically disordered NUPs line the scaffold and extend into the central channel, where they interact with cargo complexes. The NPC architecture is highly dynamic. It responds to changes in nuclear envelope tension with conformational breathing that manifests in dilation and constriction movements. Elucidating the scaffold architecture, ultimately at atomic resolution, will be important for gaining a more precise understanding of NPC function and dynamics but imposes a substantial challenge for structural biologists.

RATIONALE: Considerable progress has been made toward this goal by a joint effort in the field. A synergistic combination of complementary approaches has turned out to be critical. In situ structural biology techniques were used to reveal the overall layout of the NPC scaffold that defines the spatial reference for molecular modeling. High-resolution structures of many NUPs were determined in vitro. Proteomic analysis and extensive biochemical work unraveled the interaction network of NUPs. Integrative modeling has been used to combine the different types of data, resulting in a rough outline of the NPC scaffold. Previous structural models of the human NPC, however, were patchy and limited in accuracy owing to several challenges: (i) Many of the high-resolution structures of individual NUPs have been solved from distantly related species and, consequently, do not comprehensively cover their human counterparts. (ii) The scaffold is interconnected by a set of intrinsically disordered linker NUPs that are not straightforwardly accessible to common structural biology techniques. (iii) The NPC



A 70-MDa model of the human nuclear pore complex scaffold architecture. The structural model of the human NPC scaffold is shown for the constricted state as a cut-away view. High-resolution models are color coded according to nucleoporin subcomplex membership. The nuclear envelope is shown as a gray surface.

scaffold intimately embraces the fused inner and outer nuclear membranes in a distinctive topology and cannot be studied in isolation. (iv) The conformational dynamics of scaffold NUPs limits the resolution achievable in structure determination.

RESULTS: In this study, we used artificial intelligence (AI)-based prediction to generate an extensive repertoire of structural models of human NUPs and their subcomplexes. The resulting models cover various domains and interfaces that so far remained structurally uncharacterized. Benchmarking against previous and unpublished x-ray and cryo-electron microscopy structures revealed unprecedented accuracy. We obtained well-resolved cryoelectron tomographic maps of both the constricted and dilated conformational states of the human NPC. Using integrative modeling, we fitted the structural models of individual NUPs into the cryo-electron microscopy maps. We explicitly included several linker NUPs and traced their trajectory through the NPC scaffold. We elucidated in great detail how membrane-associated and transmembrane NUPs are distributed across the fusion topology of both nuclear membranes. The resulting architectural model increases the structural coverage of the human NPC scaffold by about twofold. We extensively validated our model against both earlier and new experimental data. The completeness of our model has enabled microsecond-long coarse-grained molecular dynamics simulations of the NPC scaffold within an explicit membrane environment and solvent. These simulations reveal that the NPC scaffold prevents the constriction of the otherwise stable double-membrane fusion pore to small diameters in the absence of membrane tension.

CONCLUSION: Our 70-MDa atomically resolved model covers >90% of the human NPC scaffold. It captures conformational changes that occur during dilation and constriction. It also reveals the precise anchoring sites for intrinsically disordered NUPs, the identification of which is a prerequisite for a complete and dynamic model of the NPC. Our study exemplifies how AI-based structure prediction may accelerate the elucidation of subcellular architecture at atomic resolution.

The list of author affiliations is available in the full article online. *Corresponding author. Email: gerhard.hummer@biophys.mpg.de (G.H.); jan.kosinski@embl.de (J.K.); martin.beck@biophys.mpg.de (M.B.)

†These authors contributed equally to this work. Cite this article as S. Mosalaganti et al., Science 376, eabm9506 (2022). DOI: 10.1126/science.abm9506



READ THE FULL ARTICLE AT

https://doi.org/10.1126/science.abm9506

RESEARCH ARTICLE

NUCLEAR PORE COMPLEX

Al-based structure prediction empowers integrative structural analysis of human nuclear pores

Shyamal Mosalaganti^{1,2,3}†, Agnieszka Obarska-Kosinska^{1,4}†, Marc Siggel^{4,5,6}†, Reiya Taniguchi^{1,2}, Beata Turoňová^{1,2}, Christian E. Zimmerli^{1,2}, Katarzyna Buczak²‡, Florian H. Schmidt²§, Erica Margiotta^{1,2}, Marie-Therese Mackmull²¶, Wim J. H. Hagen², Gerhard Hummer^{5,7}*, Jan Kosinski^{2,4,6}*. Martin Beck^{1,2}*

Nuclear pore complexes (NPCs) mediate nucleocytoplasmic transport. Their intricate 120-megadalton architecture remains incompletely understood. Here, we report a 70-megadalton model of the human NPC scaffold with explicit membrane and in multiple conformational states. We combined artificial intelligence (AI)-based structure prediction with in situ and in cellulo cryo-electron tomography and integrative modeling. We show that linker nucleoporins spatially organize the scaffold within and across subcomplexes to establish the higher-order structure. Microsecond-long molecular dynamics simulations suggest that the scaffold is not required to stabilize the inner and outer nuclear membrane fusion but rather widens the central pore. Our work exemplifies how AI-based modeling can be integrated with in situ structural biology to understand subcellular architecture across spatial organization levels.

uclear pore complexes (NPCs) are essential for transport between the nucleus and cytoplasm and are critical for many other cellular processes in eukaryotes (1-4). Analysis of the structure and dynamics of the NPC at high resolution has been a long-standing goal toward a better molecular understanding of NPC function. These investigations have proven challenging because of the sheer size of NPCs and their compositional and architectural complexity. With a molecular weight of ~120 MDa, NPCs form an extensive 120-nm-wide protein scaffold of three stacked rings: two outer ringsthe cytoplasmic ring (CR) and the nuclear ring (NR)-and the inner ring (IR). Each ring comprises eight spokes that surround a 40- to 50-nm-wide transport channel (5, 6). A single human NPC contains ~1000 copies of ~30 distinct nucleoporins (NUPs). These NUPs arrange

into multiple subcomplexes, most prominently the so-called Y-complex (7) arranged in a headto-tail orientation within the outer rings (8). The assembly of individual subcomplexes into the higher-order structure is facilitated by an as yet incompletely characterized network of short linear motifs (SLiMs) embedded into flexible NUP linkers (9-13), which have been conceived of as a molecular glue that stabilizes the scaffold. Complicating things further, the assembled scaffold is embedded into the nuclear envelope (NE). Components of the NPC scaffold interact with the NE via amphipathic helices and transmembrane domains and are believed to stabilize the fusion of the inner and the outer nuclear membranes (INM and ONM, respectively) (14, 15). Finally, the FG-NUPs grafted to the scaffold form the permeability barrier filling the central channel (16-18). Their intrinsically disordered phenylalanine-glycine (FG)-rich domains challenge traditional structural biology methods.

Owing to these intricacies, the current structural models have severe shortcomings. In the case of human NPC, only 16 NUPs, accounting for ~35 MDa (30%) of the molecular weight of the complex, are included in the models (11, 19, 20). Although the repertoire of atomically resolved structures of NUPs has grown tremendously (5, 6), said structures often have gaps in their sequence coverage, whereas homology models used by many studies have intrinsic inaccuracies. For some NUPs, no structures or homology models are available. Also, structural models put forward for other species are either incomplete or have limited precision (11, 12, 19, 21-23). Moreover, the NPCs from many other species have a vastly reduced architectural complexity, which limits their usefulness for studying human biology (12, 22–25). The exact grafting sites for FG-NUPs, which are crucial for understanding the transport mechanism, remain elusive. How exactly the NPC scaffold is anchored to the membrane, how it responds to mechanical cues imposed by the nuclear envelope, and if and how it contributes to shaping the membrane remain unknown. Finally, the models are static snapshots that do not take conformational dynamics into account.

In this study, we combined cryo-electron tomography (cryo-ET) analysis of the human NPC from isolated NEs and within intact cells with artificial intelligence (AI)-based structural prediction to infer a model of >90% of the human NPC scaffold at unprecedented precision and in multiple conformations. We demonstrate that AI-based models of NUPs and their subcomplexes built using AlphaFold (26) and RoseTTAfold (27) are consistent with unreleased x-ray crystallography structures, cryo-electron microscopy (cryo-EM) maps, and complementary data. We elucidate the three-dimensional (3D) trajectory of linker NUPs, the organization of membrane-binding domains, and grafting sites of most FG-NUPs in both the constricted and dilated conformations.

Results

A 70-MDa model of the human NPC scaffold

The completeness of the previous structural models of the human NPC was limited by the resolution of the available EM maps in both the constricted and the dilated states and by the lack of atomic structures for several NUPs (19-21). To improve the resolution of the constricted state of the NPC, we subjected nuclear envelopes purified from HeLa cells to cryo-ET analysis, as described previously (19, 21). We collected an approximately fivefold larger dataset than what we previously published and applied a newly developed geometrically restrained classification procedure (see Materials and methods). These improvements resulted in EM maps with resolutions of 12, 12.6, and 23.2 Å, respectively, for the CR, IR, and NR (figs. S1 to S3). Next, we obtained an in cellulo cryo-ET map of dilated human NPCs in the native cellular environment within intact HeLa and human embryonic kidney 293 (HEK293) cells subjected to cryo-focused ion beam (cryo-FIB) specimen thinning (fig. S1). The dilated in cellulo NPC exhibits an IR diameter of 54 Å, compared with 42 Å in the constricted state, consistent with previous work in U2OS (28), HeLa (29), SupT1 (30), and, most recently, DLD-1 cells (20). In contrast to other species, there is no compaction along the nucleocytoplasmic axis during dilation (fig. S2) (23, 25). The quality of our in cellulo map is sufficient to discern the structural features known from the constricted state, such as a double head-to-tail arrangement of Y-complexes,

¹Department of Molecular Sociology, Max Planck Institute of Biophysics, 60438 Frankfurt am Main, Germany.
²Structural and Computational Biology Unit, European Molecular Biology Laboratory, 69117 Heidelberg, Germany.
³Life Sciences Institute and Department of Cell and Developmental Biology, University of Michigan, Ann Arbor, MI 48109, USA.
⁴European Molecular Biology Laboratory Hamburg, 22607 Hamburg, Germany.
⁵Department of Theoretical Biophysics, Max Planck Institute of Biophysics, 60438 Frankfurt am Main, Germany.
⁶Centre for Structural Systems Biology, 22607 Hamburg, Germany.
⁷Institute of Biophysics, Goethe University Frankfurt, 60438 Frankfurt am Main, Germany.

*Corresponding author. Email: gerhard.hummer@biophys.mpg.de (G.H.); jan.kosinski@embl.de (J.K.); martin.beck@biophys.mpg.de (M.B.)

†These authors contributed equally to this work. ‡Present address: Proteomics Core Facility, Biozentrum, University of Basel, CH-4056 Basel, Switzerland. §Present address: Institute of Science and Technology Austria, 3400 Klosterneuburg, Austria. ¶Present address: Institute of Molecular Systems Biology, Department of Biology, ETH Zurich, Zurich, Switzerland.

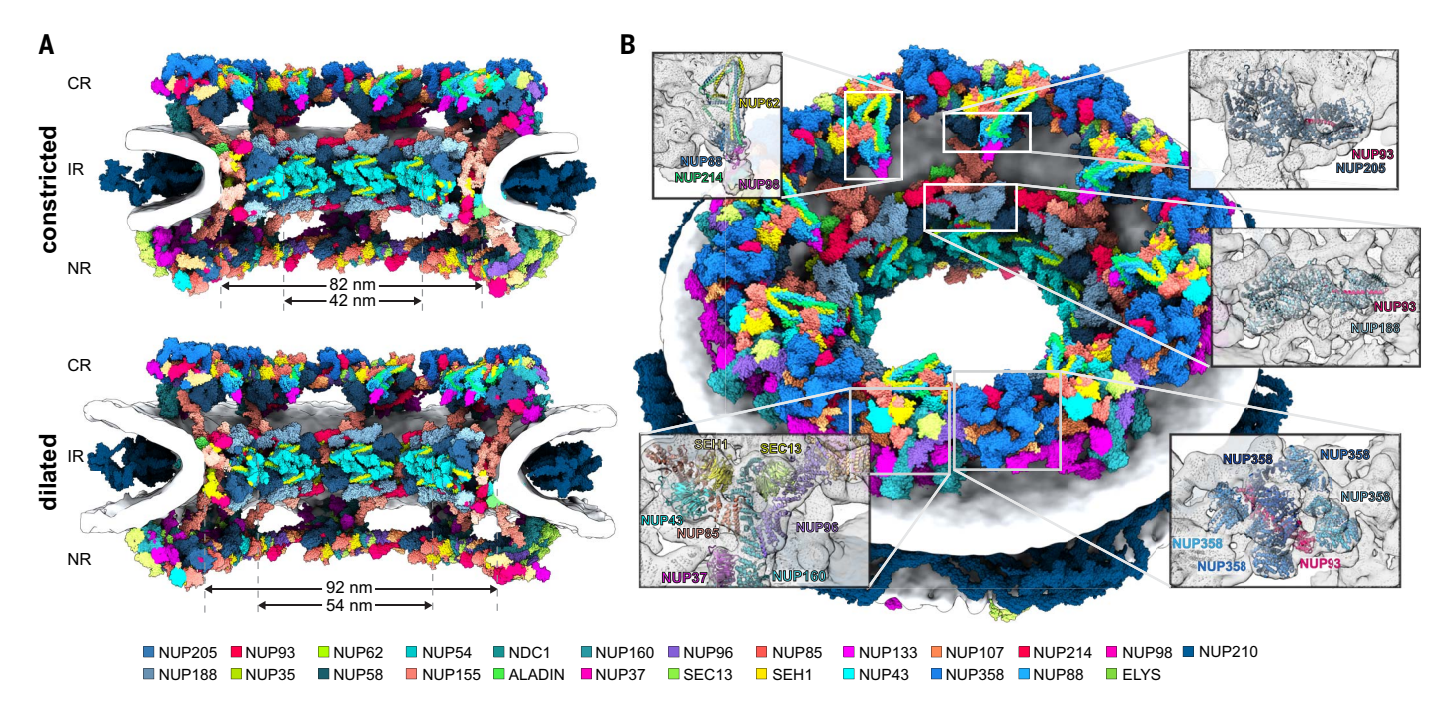


Fig. 1. Scaffold architecture of the human NPC. (A) The near-complete model of the human NPC scaffold is shown for the constricted and dilated states as cutaway views. High-resolution models are color coded as indicated in the color bar. The nuclear envelope is shown as a gray isosurface. (B) Same as (A), but shown from the cytoplasmic side for the constricted NPC. The insets show individual features of the CR and IR enlarged with secondary structures displayed as cartoons and superimposed with the isosurface-rendered cryo-ET map of the human NPC (gray).

IR subunits, and inter-ring connectors. We observe an increase in the distance between the adjacent spokes within the IR, in agreement with previous cryo-ET maps of NPCs (20, 22, 23, 25).

To generate a comprehensive set of structural models of human NUPs, we used the recently published protein structure prediction software AlphaFold (26) and RoseTTAfold (27). We found that most of the NUPs can be modeled with high confidence scores (fig. S5 and table S1). In addition, we validated the accuracy of the models by comparison to structures from accompanying publications (31, 32) of human NUP358, NUP93, NUP88, and NUP98 and of Nup205 and Nup188 from Chaetomium thermophilum (fig. S6 and table S1). These structures were not used as input for the modeling procedure. The AI-based models also excellently fit our EM densities, with significant P values and high crosscorrelation scores (fig. S7, A to E). Furthermore, we used single-particle cryo-EM to determine the experimental structure of human NUP155 (fig. S8, A to C) and validated the respective AlphaFold model. Although the model and the structure do not perfectly superpose as whole chains owing to the flexibility of the protein, their local tertiary structures and sidechain conformations are highly similar [global LDDT (local distance difference test) score of 91.6] (fig. S9). Notably, the loops that were not resolved in the experimentally derived structure consistently show low predicted LDDT

(pLDDT) scores (fig. S9B), further supporting the reliability of this metric.

With full-length models at hand, we could identify the positions of NUP205 and NUP188 within the scaffold, which had not been unambiguously determined in the previous human NPC (hNPC) cryo-ET maps. The AI-predicted conformation of the N-terminal domain of NUP358 fits the observed EM density better than the two x-ray structures (fig. S7H). The NUP358 localization is in agreement with previous analysis (21) and α -helical densities visible in the Xenopus EM map (33) (fig. S10). The full-length model of the protein ELYS, for which thus far only the N-terminal β-propeller could be placed (21), fits the EM map as a rigid body (fig. S7E) and confirms its binding site to each of the Y-complexes in the NR. The models of NUPs in the CR agree with the secondary structure observed in the Xenopus cryo-EM map (fig. S10).

The capacity of AI-based structure prediction tools to identify and model protein interfaces with high accuracy has recently been demonstrated (34-36). We therefore attempted to model NUP interfaces using the ColabFold software, a version of AlphaFold adopted for modeling protein complexes (35). We found that ColabFold predicted several NUP subcomplexes with interdomain confidence scores that correlated with the accuracy of the models, while negative controls with nonspecific interactions yielded low confidence models (figs. S11 to S14). The models of these subcomplexes not only reproduced their respective, already available x-ray structures but also agreed with newly resolved x-ray structures (31, 32) (tables S1 and S2) and exhibited physical parameters similar to real interfaces (table S3). Specifically, x-ray structures of C. thermophilum Nup205 and Nup188 in complex with Nup93 as well as Nup93 in complex with Nup35 are consistent with the human ColabFold model (fig. S6 and table S2). These structures represent proteins in complex with the respective SLiMs and form relatively small interfaces. However, for larger subcomplexes we also obtained structural models that convincingly fit our cryo-ET maps (fig. S14). For example, the structure predicted for the so-called central hub of the Y-complex was consistent with the organization seen in fungal x-ray structures and explained additional density within the cryo-ET map specific to the human NPC. Our model of the Y-complex hub includes a previously unknown interaction between NUP96 and NUP160 (fig. S11). ColabFold built a model of the NUP62 complex that has high structural similarity to the fungal homolog (table S2) and fits the EM map with significant P values (fig. S14), even though no structural templates were used for modeling. We were also able to obtain a trimeric model of the small arm of the Y-complex comprising NUP85, SEH1, and NUP43. The model fits the EM map with significant P values, confirming the known structure of NUP85-SEH1 interaction (table S2) and revealing how NUP43 interacts with NUP85 (fig. S14). In the case of the NUP214 complex, for which no structures are available, the ColabFold model is highly consistent with the rather distinctively shaped EM density (fig. S14). The interface between NUP214 and NUP88 that is biochemically validated in (31) has also been predicted with high structural similarity to the equivalent interface between homologs from *C. thermophilum* and budding yeast (table S2).

With the cryo-EM maps and the repertoire of structural models of individual NUPs and their subcomplexes, we built a nearly complete model of the human NPC scaffold (Fig. 1A; supplementary text in the supplementary materials; and Materials and methods). The individual components are detailed in table S4. We used the previous model (19, 21) as a reference for modeling the scaffold of the constricted state and replaced all previously fitted domains with human AlphaFold and ColabFold models. We then added the remaining newly modeled subunits by systematic fitting to the EM map and refinement using Assembline (37) (figs. S14 and S15). In addition to fitting the models, we added several disordered linkers that connect spatially separated domains and SLiMs within the NPC (figs. S16 to S18). We then built the model of the dilated state by fitting the constricted NPC model into the dilated NPC map and refining the fits using Assembline. The resulting models (Fig. 1) include 25 of the ~30 human NUPs (fig. S19 and table S4). The protein regions explicitly included in the models account for 70 MDa of the molecular weight of the NPC (>90% of the scaffold molecular weight), compared with 16 NUPs and 35 MDa (46% of the scaffold weight) of the previous model, and largely account for the EM density observed in the constricted and dilated states.

This model yields new insights into the organization of the human NPC (Fig. 1). Within the IR, NUP188 and NUP205 localize to the outer and inner subcomplexes, respectively, consistent with previous analysis in other species (12, 22, 23). Furthermore, we localized two copies of NUP205 in the CR and one in the NR (33), thus resolving previous ambiguities (11, 19, 21). Two previously undetected copies of NUP93 bridge the inner and outer Ycomplexes in both the CR and NR, with an inherent C2 symmetry. This observation is consistent with biochemical experiments that initially identified interactors of NUP93 in the outer rings (38). The copy of NUP93 in the CR is located underneath the NUP358 complex. further corroborating a role of NUP358 in stabilizing the higher-order structure (21). Yet another copy of NUP93 that is specific to the CR bridges the inner Y-complexes from two consecutive spokes. This is consistent with an additional copy of NUP205 in the CR as compared with the NR, because NUP93 and NUP205 heterodimerize through a SLiM within the extended N terminus of NUP93 (see next section; fig. S10) (31, 32). The AI-based model of the NUP214 subcomplex interacts with NUP85, which points toward the central channel, likely to optimally position the associated helicase that is crucial for mRNA export.

Linker NUPs fulfill dedicated roles of spatial organization within the higher-order assembly

Because the exact 3D trajectory of the linkers through the NPC scaffold was unknown, it remained difficult to understand their precise structural role beyond conceptualization as molecular glue. In our model, AI-based models of human NUP-SLiM subcomplexes allowed us to map the anchor points of the linkers to the scaffold. The AI-based models correctly recapitulated SLiM interactions known from x-ray structures but also revealed previously unknown human NUP-SLiM interactions. In comparison to the x-ray structures, the AI-based models more extensively covered the structured domains, thus reducing the length of the linkers and restricting their possible conformational freedom within our model.

To generate a connectivity map of the NUP linkers (Fig. 2), we used a multistep procedure. First, we calculated all geometrically possible connections. Next, we eliminated linker combinations that were too distant, caused steric clashes, or were combinatorially impossible. Finally, we used Assembline to model the remaining linkers in explicit atomic representation for both constricted and dilated states (Fig. 2, figs. S16 to S18, supplementary text, and Materials and methods).

The resulting connectivity map (Fig. 2A) reveals that the NUP35 linker regions bridge neighboring spokes of the IR. In our model, the NUP35 dimer is positioned into previously unassigned EM density between spokes (fig. S14), and each of the two copies reaches out with its SLiMs to NUP155 and NUP93 of the adjacent spokes (Fig. 2A and fig. S16). The NUP35 dimer, which is critical during early NPC biogenesis (39), thus functions as an architectural organizer for the IR membrane coat in a horizontal direction along the membrane plane.

In contrast, the connectivity map demonstrates that the linkers at the N terminus of the NUP93 copies that connect anchor points at NUP205 or NUP188, and NUP62 complex in the IR, cannot reach across spokes and thus connect subunits within a single IR subcomplex inside of the same spoke (fig. S17). Thereby, the two outer copies bind to NUP188, while the two inner copies bind to NUP205. Thus, NUP93 acts as an architectural organizer within, but not across, spokes.

In the CR and NR, the linkage between NUP93 and NUP205 is geometrically possible (fig. S18). This linkage suggests the similar

architectural design of the respective complexes in which the NUP93 SLiM that binds the NUP62 complex could also facilitate linkage to the homologous NUP214 complex, although the corresponding structural information is still missing. The duplication of NUP205 and NUP93 in the CR is suggestive of yet another copy of the NUP214 complex that is not well resolved in the cryo-EM map of the constricted state and thus remains to be further investigated. This analysis is consistent with the biochemical analysis and structural modeling in the accompanying publication (32). In conclusion, the individual linker NUPs specialize in dedicated spatial organization functions responsible for distinct aspects of assembly and maintenance of the NPC scaffold architecture.

A transmembrane interaction hub organizes the interface between outer and inner rings

Several types of structural motifs associate the NPC scaffold with the membrane. The spatial distribution of the amphipathic helices and membrane-binding loops harbored by NUP160, NUP155, and NUP133 across the scaffold has been previously revealed (19). The analysis of the protein linkers in our model allowed the mapping of an approximate location of the amphipathic helices of NUP35. In addition to these motifs, the human NPC contains three transmembrane NUPs, the precise location of which remains unknown.

Among the three human transmembrane proteins, NDC1 is the only one that is conserved across eukaryotes (40). NDC1 is known to interact with the poorly characterized scaffold NUP ALADIN (41, 42). We confirmed this interaction using proximity labeling mass spectrometry with BirA-tagged ALADIN and identified NDC1 and NUP35 as the most prominently enriched interactors (fig. S20). NDC1 is predicted to comprise six transmembrane helices followed by a cytosolic domain containing mainly α helices, whereas ALADIN is predicted to have a β-propeller fold. Structures of both NDC1 and ALADIN, however, remain unknown. Using AlphaFold/ Colabfold, we could model the structures both as monomers and a heterodimeric complex with high-confidence scores (figs. S5 and S11). Systematic fitting of the heterodimeric models to the EM map unambiguously identified two locations within the IR (fig. S14). The EM density was not used as a restraint for modeling, but it matches the structure of the model and is consistent with the only patches of density spanning the bilayer (Fig. 3, fig. S14, and supplementary text), therefore further validating the model. The two locations are C2-symmetrically equivalent across the nuclear envelope plane, thus assigning two copies of ALADIN and NDC1 per spoke, corroborating experimentally determined stoichiometry (43). The identified locations are close to the

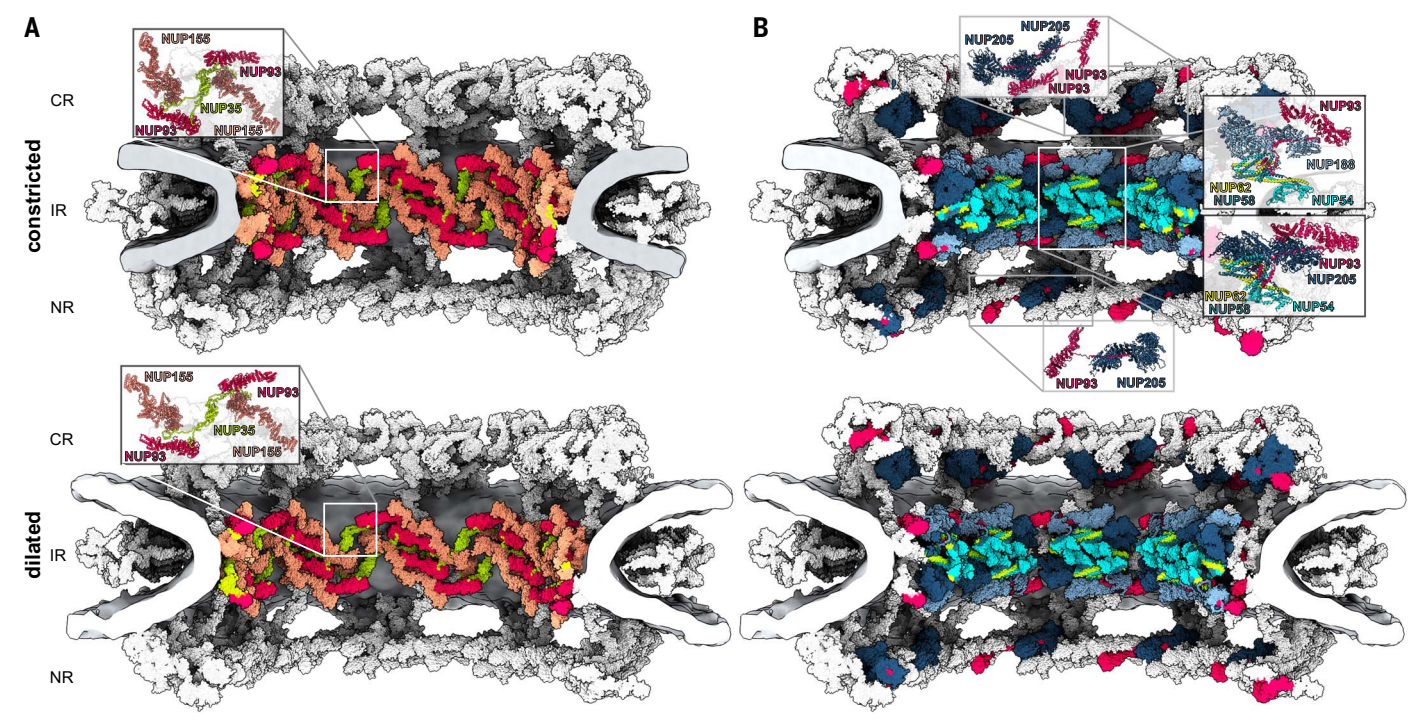


Fig. 2. The connectivity of protein linkers within the human NPC. (A) The NUP35 dimer interconnects adjacent spokes across different subcomplex species, thus facilitating cylindrical assembly of the IR in both constricted (top) and dilated (bottom) states. The NUP205, NUP188, NUP62 complex, and the N terminus (amino acids 1 to 170) of NUP93 are hidden from view to expose NUP35. (B) The N terminus of NUP93 isostoichiometrically

connects the subunits NUP205, NUP188, NUP62, NUP58, and NUP54 within the same subcomplex species. Insets show NUP93 connectivity, highlighting its interaction with two copies of NUP205 in the CR, two copies each with NUP205 and NUP188 in the IR, and a single copy of NUP205 in the NR. The respective subunits are color coded as in Fig. 1, while all other subunits and the nuclear membranes are shown in gray.

membrane-binding N-terminal domains of NUP155 and amphipathic helices of NUP35. which is also consistent with our proximity labeling data (fig. S11) and previous functional analysis (44). The proximity labeling data prominently identified Gle1, which was previously shown to interact with NUP155 (45). Using AlphaFold, we predicted an interaction between the C terminus of NUP155 and the N-terminal SLiM in Gle1 with high confidence scores (fig. S20B). We also predicted an ALADIN-binding SLiM in NUP35, located between the amphipathic helix and NUP155binding SLiM (Fig. 3 and fig. S11). We therefore propose that, together with NUP155, NUP35, ALADIN, and NDC1 form a transmembrane interaction hub that anchors the inner membrane coat of the IR and orients the NUP155 connectors toward the outer rings. The central position of ALADIN within the NPC might explain functional consequences of mutations in ALADIN that are implicated in triple A syndrome (46-48) and is consistent with the absence of ALADIN in fungi, which lack the NUP155 connectors (24).

We next examined the structure of NUP210, which contains a single-pass transmembrane helix and is the only NUP that primarily resides in the NE lumen. This NUP is composed of multiple immunoglobin-like domains

and is thought to form a ring around the NPC within the NE lumen (49), but the structure of the ring has only been modeled in fungi. We used RoseTTAfold to model full-length NUP210 and obtained an elongated model with clearly defined interfaces between consecutive domains. This model fitted the density sufficiently well to allow tracing NUP210 monomers in the cryo-EM map of the Xenopus laevis NPC, which is superbly resolved in the luminal region (50). Thus, we could assign eight copies of NUP210 per spoke (fig. S21). Modeling of individual NUP210 fragments and inter-NUP210 interactions with AlphaFold/ ColabFold (fig. S21 and table S1) led to a composite model that explained the entire density of the luminal ring of the human and Xenopus cryo-EM maps, including the C-terminal transmembrane helix. The helix is long enough to span the NE and reaches the IR in the vicinity of the NDC1/ALADIN/NUP155/NUP35 transmembrane interaction hub. This location is consistent with known interactions of NUP210 homologs (51) and our proximity labeling data (fig. S20). The model of the NUP210 ring also matches the luminal density visible in our in cellulo EM map, allowing us to model the ring in the context of both constricted and dilated NPC (Fig. 1 and fig. S21). To further confirm the NUP210 assignment in human cells, we deleted NUP210 in HEK293 cells using CRISPR-Cas9 and analyzed the structure of the NPCs in cellulo using cryo-ET. The resulting map indeed showed a lack of the luminal ring density (fig. S4). The NPC scaffold in the resulting map appears unchanged overall, including its diameter, suggesting the NUP210 is not required for faithful NPC assembly.

Our model includes all known membranebinding domains except for the cell typespecifically expressed POM121-the precise location of which remains unknown within the NPC, and neither AlphaFold nor RoseTTAfold could build structural models with high confidence. The resulting membrane association map reveals that the membrane-binding β-propellers of the Y-complex (NUP160 and NUP133) and the IR (NUP155) are distributed as multiple pairs over the entire scaffold, whereby they follow a well-defined pattern. They form an overall Z-shaped outline within an individual spoke (Fig. 3). The NDC1/ALADIN/NUP155/ NUP35 membrane-binding hub is situated at the interface of the IR with the outer rings and is distinct from the additional NUP155 pair at the NE symmetry plane. The membranebinding motifs arrange in similar clusters in both the constricted and dilated state. Their relative arrangement does not change uniformly

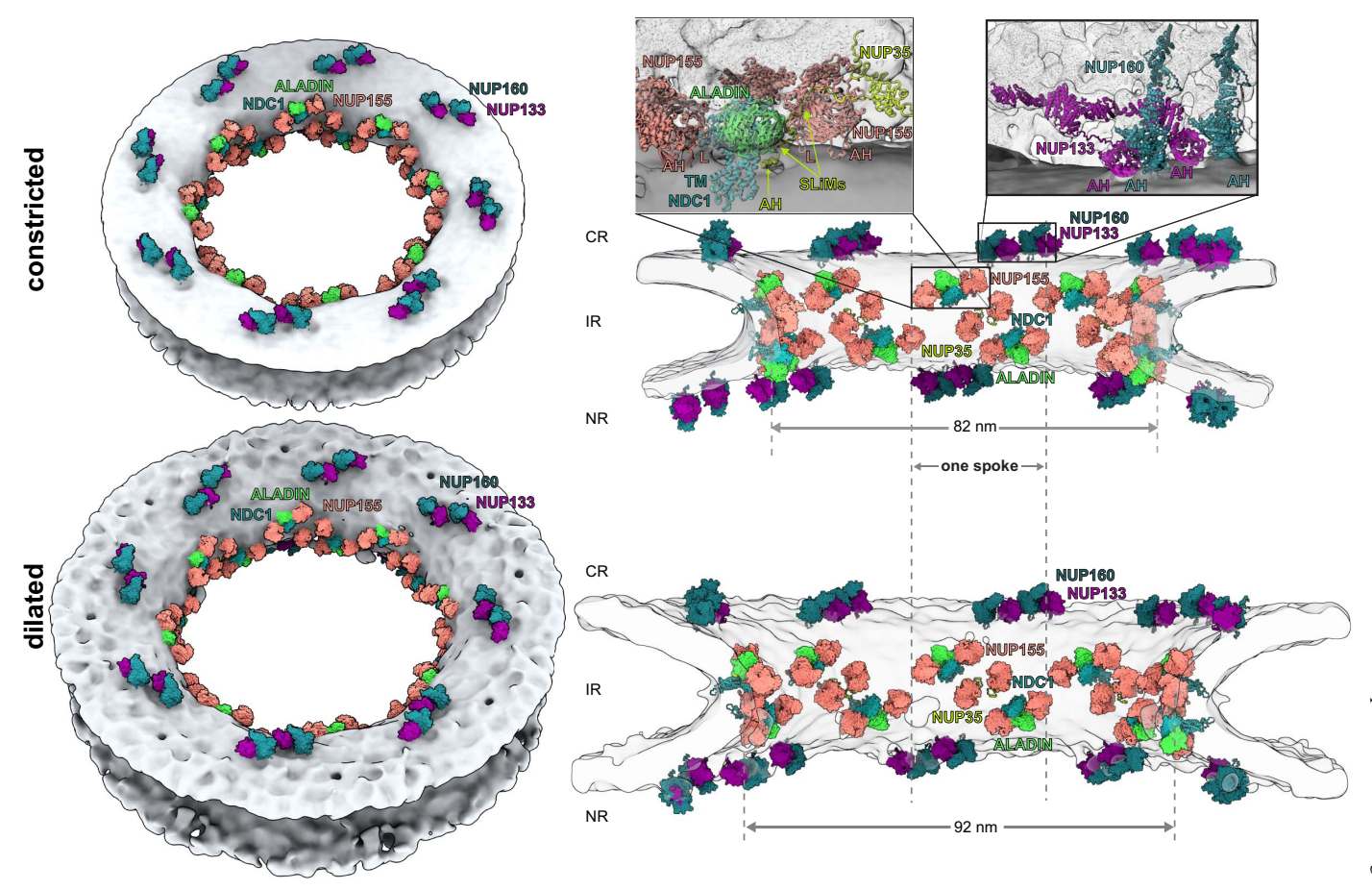


Fig. 3. The membrane-anchoring motifs of the human NPC are distributed over the entire scaffold. The membrane-binding β-propellers of the Y-complex and IR complex are shown color coded and arranged as pairs of the respective inner and outer copies. ALADIN and NDC1 form a transmembrane interaction hub with the inner and connector copies of NUP155, which is shown enlarged in the inset in the cut-away side view (right). The nuclear membranes are shown as a gray isosurface. AH, amphipathic α helix; L, loop; TM, transmembrane; SLiMs, short linear motifs.

during dilation, rather the relative distances within the spokes remain constant while the spacing of the spokes increases (Fig. 3).

The NPC scaffold prevents membrane constriction in the absence of membrane tension

It has been a long-standing view that the scaffold architecture of the NPC has evolved distinct membrane-binding motifs to stabilize the membrane at the fusion of the INM and ONM (14, 52). To test the contribution of the scaffold architecture to membrane curvature, we used molecular dynamics (MD) simulations using a coarse-grained Martini force field (53, 54). We first simulated a doublemembrane pore without proteins with an initial pore diameter and membrane spacing as seen in the constricted NPC cryo-ET map. We found that the pore constricts during 1-us simulations and stabilizes once the radii of the INM or ONM and the NE hole are the same, such that the mean curvature nearly vanishes (Fig. 4A, fig. S23, and Movie 1). This is in line with Helfrich membrane elastic theory, which predicts a catenoid-like pore shape with equal radii of curvature at the pore center as the lowest energy structure, and an energetic cost of ~500 kJ/mol to widen the pore (supplementary text). Notably, the opening of the relaxed double-membrane pore is considerably smaller than even the most constricted NPC conformation. The NPC scaffold thus keeps the pore wider than it would be without the scaffold.

These findings would predict that the nuclear membranes push against the NPC scaffold even in the most constricted state. which is in agreement with experimental data (23). To examine the effects of this tension on the NPC, we generated an NPC scaffold model with explicit membrane and water as a solvent and ran 1-us MD simulations (Fig. 4B. figs. S23 to S27, and Movies 2 and 3). We omitted the luminal NUP210 and focused our analysis on the architecturally important NR, CR, and IR. In these simulations, we found that the membrane pore wrapped tightly around the IR plane, adopting an octagonal shape (Fig. 4C). Similarly tight wrapping and octagonal shapes have been seen in the previous EM analyses of NPCs (21, 55, 56). We also observed that the diameter of the NPC scaffold constricted by ~9% (Fig. 4B). We attribute this tightening primarily to mechanical tension in the pore widened beyond the catenoid shape. First, we observed similar contraction in simulations with rescaled protein-protein interactions (fig. S27). Second, by applying lateral tension on the double membrane, we could maintain the pore width or widen it (Fig. 4B and fig. S23B). At even higher tension, the membrane spontaneously detached from the NPC scaffold (fig. S28). Taken together, our data support a model in which the role of the NPC scaffold is not to stabilize the membrane fusion per se but rather to widen the diameter of the membrane hole without necessitating a wider envelope.

Discussion

We have built a 70-MDa model of the human NPC scaffold in the constricted state (smaller diameter) as adopted in purified nuclear envelopes and in the dilated state as adopted in cells, whereby recent work in fungi has identified constricted NPCs inside of cells under

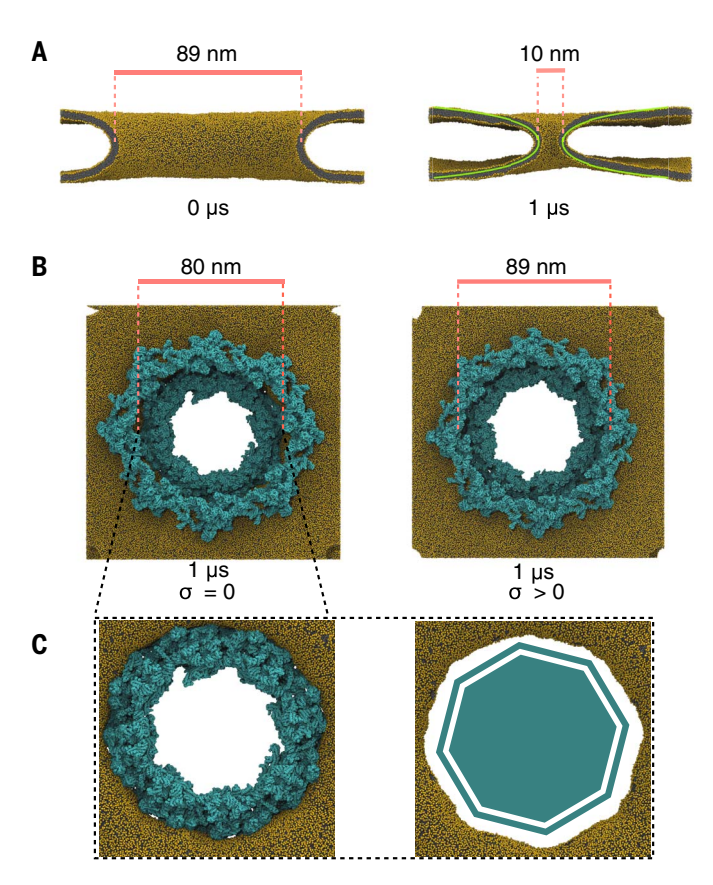


Fig. 4. Dynamics of the NPC from molecular simulations. (A) An isolated half-toroidal double-membrane pore shaped initially as in the tomographic structure of the constricted NPC (left) tightens over the course of 1 µs of MD (right) toward the catenoid-like shape (green) predicted by membrane elastic theory. Shown are cuts along the axis of the double-membrane pore with lipid headgroups and tails in gold and gray, respectively. The solvent is not shown. (B) The NPC (cyan) widens by ~10% in response to lateral membrane tension (right; $\Delta P = 2$ bar) compared with a zero-tension simulation (left; $\Delta P = 0$). Shown are snapshots of the relaxed structures after 1 µs of MD. (C) The membrane fits tightly around the NPC inner ring (cyan, left; $\Delta P = 0$) and forms an octagonally shaped pore (right, NPC not shown).

specific physiological conditions (23). Our model includes multiple previously unassigned domains and proteins, resolves long-standing ambiguities in alternative NUP assignments, lays out a connectivity map of the protein linkers across the NPC scaffold, maps out the membrane-anchoring motifs, and provides a high-quality basis for further investigations of NPC dynamics and function. Our analysis demonstrates that our model is sufficiently complete for molecular simulations, which in the future could quantitively and predictively describe how the NPC interplays with the nuclear membrane and how it responds to mechanical challenges. The model also provides a more accurate starting point for simulations of nucleocytoplasmic transport by providing the native constraints on the diameter and a more precise mapping of the positions where the FG tails emanate from the scaffold (fig. S22).

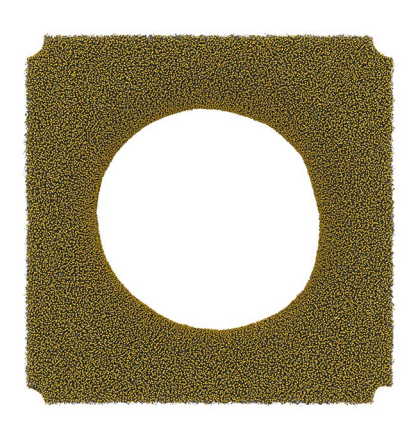
How an intricate structure consisting of ~1000 components can be faithfully assembled in the crowded cellular environment is a very

intriguing question. Our connectivity map captures the 3D trajectory of linker NUPs through the assembled scaffold. Taken together with previous analysis of NPC assembly (9-13, 19), it suggests that the linker NUPs facilitate dedicated spatial organization functions. The connections of NUP93 within individual IR complexes and to the NUP214-complex suggest a role in ensuring isostoichiometric assembly. This finding is consistent with the recent analysis of early NPC biogenesis, suggesting that NUP93 associates isostoichiometrically with the NUP62-complex already during translation in the cytosol (57). Thus, the stoichiometric assembly of the NUP62 subcomplex together with NUP205/188-NUP93 heterodimer is likely preassembled away from sites of NPC biogenesis, explaining the importance of the linker for intra-subcomplex interactions. How the spokes form a C2 symmetric interface at the NE plane remains to be addressed.

In the IR membrane coat, multiple interactions converge into a distinctive transmembrane interaction hub. We propose that its core is formed by the ALADIN-NDC1 heterodimer at the interface between the outer and inner rings. This transmembrane interaction hub is likely a spatial organizer for two proximate copies of NUP155 within the same spoke that point toward the outer rings and IR, respectively. ALADIN-NDC1 likely further associates with NUP210, which arches between spokes in the NE lumen. The hub also binds NUP35, which connects to NUP155 copies of neighboring spokes, thus facilitating the horizontal, cylindrical oligomerization. Because NUP35 associates with NUP155 early during NPC assembly (39), its dimerizing domain appears critical to scaffold its flexible linkers toward neighboring spokes within the IR membrane coat.

The often-emphasized notion that NPCs fuse the INM and ONM or that they stabilize the fusion of the INM and ONM is not necessarily supported by our analysis. Our simulations suggest that the membrane fusion topology per se is stable under certain conditions, relaxing toward a catenoid shape with zero membrane bending energy. Indeed, some species maintain the fusion topology in the absence of NPCs, for example, during semiclosed mitosis in Drosophila melanogaster (58). Our analysis instead suggests that NPCs stabilize a pore that is wider than in the relaxed, tensionless double-membrane hole. This notion agrees with the ultrastructural analysis of postmitotic NPC assembly, which has revealed that NE holes are formed at small diameters and dilate once NPC subcomplexes are recruited (59). These data argue that the membrane shape defines the outline of the NPC scaffold and not vice versa.

We use AI-based structure prediction programs AlphaFold and RoseTTAfold to model all atomic structures that were used for fitting to the EM maps. Although x-ray and cryo-EM structures were used for validation, no experimental atomic structures were directly incorporated into the model. Predicted atomic structures traditionally exhibited various inaccuracies, limiting their usage for detailed near-atomic model building in low-resolution EM maps. However, Alpha-Fold and RoseTTAfold have recently demonstrated unprecedented accuracy in predicting structures of monomeric proteins (26, 27, 60-65) and complexes (34, 36, 61, 66). They accurately assess their confidence at the level of individual residues and interdomain contacts (26, 27, 61). Indeed, we could successfully validate our models by comparing them to unpublished crystal structures, crvo-EM maps, and biochemical data. The resulting model of the NPC scaffold is almost complete and exhibits near-atomiclevel precision at several interfaces. The model also contains several peripheral NUPs, for example, parts of the NUP214 and NUP358 complexes. Projection of the locally estimated accuracy into an asymmetric unit of the NPC



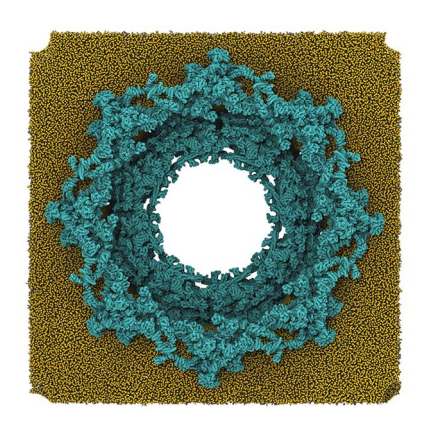
Movie 1. MD simulation of a half-toroidal double membrane. MD simulation trajectory of an isolated half-toroidal double membrane shaped initially as in the tomographic structure of the constricted NPC. The pore tightens within 1.2 µs of MD (see also Fig. 4B and fig. S23A for the diameter time trace). A top view of lipids is shown. Solvent is omitted for clarity.

reveals that the structured regions are generally modeled with good confidence, while linkers and peripheral loops are less well defined (fig. S29). Although the entire EM density for those peripheral NUPs is unlikely to be resolved in the near future owing to their flexibility, the complete model of the human NPC could be within reach by integrating data from complementary techniques that can address flexible proteins, such as super-resolution microscopy, fluorescence resonance energy transfer. and site-specific labeling (18).

Thanks to in situ and in cellulo cryo-ET and powerful AI-based prediction (26, 27), intricate structures such as the NPC can now be modeled. Not all subunit or domain combinations that we attempted to model with AI-based structure prediction led to structural models that were consistent with complementary data, emphasizing that experimental structure determination will still be required in the future for cases in which a priori knowledge remains sparse. However, even if AI-based modeling does not yield high-confidence results, the models can still serve as tools for hypothesis generation and subsequent experimental validation.

Materials and methods Mammalian cell cultivation and subcellular fractionation

Modified human embryonic kidney cells 293 (HEK Flp-In T-Rex) 293 Cell Line, Life Technologies) designed for rapid generation of stably transfected cell lines with a tetracyclineinducible expression system were used as parental cells. The NUP210 CRISPR-knockout line (HEK NUP210Δ) has been previously described (67). In general, all cells were main-



Movie 2. MD simulation of an NPC with explicit **membrane** (α = 1.0). MD simulation of the NPC (cyan) covering ~1.2 μ s with α = 1.0 (see also figs. S23 and S27 for the diameter time trace). A top view of the NPC with membrane is shown. Solvent is omitted for clarity.

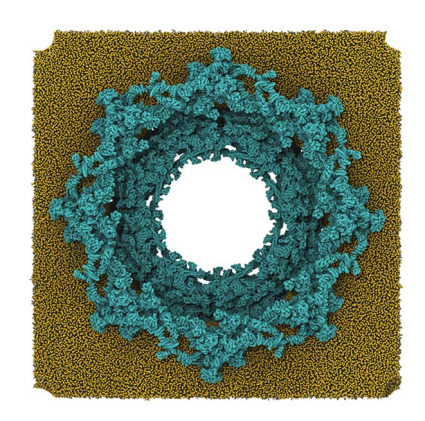
tained in Dulbecco's modified Eagle medium (DMEM) supplemented with 5 g/liter glucose and 10% heat-inactivated fetal bovine serum (FBS, Sigma-Aldrich). HeLa Kyoto cell line was maintained in DMEM medium containing 1 g/liter glucose supplemented with 2 mM L-glutamine. Cells grown close to confluency (~90%) were trypsinized with 0.25% trypsin containing EDTA (Life Technologies) and passaged for further growth. For the preparation of nuclear envelopes, HeLa cells were cultured and subjected to subcellular fraction as described before (8, 43).

Grid preparation

Grids with HeLa nuclear envelopes were prepared exactly as described in (21). For the in cellulo work, Au200 R2/1 SiO₂ grids (Quantifoil Micro Tools GmbH) were glow discharged on both sides and sterilized under ultraviolet light. In a six-well cell culture dish, either 250,000 cells per well (for HeLa) or 400,000 cells per well (HEK293) were pipetted onto the grids prewetted with DMEM medium. Cells were left to settle and attach to the grids for 4 hours at 37°C in 5% CO₂. Subsequently, the HeLa or HEK293 grids were plunge-frozen with a Leica EM GP plunger with set chamber environment to 99% humidity and 37°C. Grids were blotted from the backside for 2 s and plunged in liquid ethane-propane mix (37 and 63%) at about −195°C. HEK NUP210∆ grids were washed once with phosphate-buffered saline containing 8% dextran (35.45 kDa) and blotted for 3 s before plunge freezing in -186°C liquid ethane.

Cryo-FIB milling and data acquisition

Plunge-frozen sample grids were FIB-milled on an Aquilos FIB-SEM (Thermo Fisher Scientific)



Movie 3. MD simulation of an NPC with explicit **membrane** (α = 0.7). MD simulation of the NPC (cyan) covering $\sim 1.2 \, \mu s$ with $\alpha = 0.7$ (see also Fig. 4B and fig. S23A for the diameter time trace). A top view of the NPC with membrane is shown. Solvent is omitted for clarity.

as described before (22, 23). In brief, samples were coated with inorganic platinum (Ptsputtering). Subsequently, a protective layer of organometallic platinum was deposited for ~20 s using the gas injection system. Cells were then stepwise milled at a 20° angle to a final thickness of ~200 to 250 nm using decreasing ion-beam currents of 1 nA to 50 pA. A final round of Pt-sputtering was applied before unloading the sample.

Cryo-electron tomography and subtomogram averaging of the human NPC from nuclear envelopes

Tilt series were collected with SerialEM as described by Kosinski et al. (19). The angular coverage of the tilts spanned from -60° to +60°. Ten 8K x 8K frames, per tilt, were collected in the super-resolution mode on a K2 direct electron detector (Gatan Inc.) equipped with an BioQuantum Imaging Filter (GIF). An average total dose of 120 e⁻/Å² per tomogram was used. Five hundred sixteen new tilt series were collected and combined with 101 tilt series reported by Kosinski et al. (19) leading to a total of 617 tilt series. Incomplete tilt series (missing more than seven tilts in either direction or terminated owing to autofocusing error because of the edge of the grid bar) were discarded. Contrast transfer function (CTF) was determined using CTFFind4 (68). Tilt series with large discrepancies in the two defocus values estimated by CTFFind4 were also removed. This resulted in a total of 554 tilt series. Tilt series were manually aligned by tracking gold fiducials in IMOD (69). Tilt series were filtered according to accumulated exposure on the basis of parameters described by Kosinski et al. (19). Tilt series were reconstructed with 3D CTF correction using NovaCTF (70).

Subtomograms (7711) containing individual NPCs were extracted, corresponding to 61,688 asymmetric units. The pixel size at the specimen level was 3.37 Å. Tomograms were binned by Fourier cropping 2× (bin2), 4× (bin4), and 8× (bin8), and subtomograms were extracted at each level of binning corresponding to a pixel size of 6.74, 13.48, and 26.96, respectively. Subtomogram averaging was performed on a whole-pore level with the bin8 dataset. Subsequently, asymmetric units were extracted from the aligned pores and averaged as described by Kosinski et al. (19). Subunits with the center outside of tomogram boundaries were excluded from further processing. The CR, IR, and NR were processed separately. that is, the positions of subunit centers were moved to be in the center of each ring, resulting in three different sets of subtomograms. Rings with the center outside of tomogram boundaries were excluded from further processing. The subtomograms were iteratively aligned first on bin4 and then on bin2 level, and the final alignment was refined on bin1 level. The complete subtomogram averaging and alignment was performed using novaSTA (71), the masks necessary for the alignment were created in Dynamo (72) and Relion (73).

After the bin4 alignment, the quality of each subtomogram was assessed using geometrically restrained classification that is based on the expected geometrical shape of a complete ring. More precisely, the subunits corresponding to one NPC ring should still be part of a ring after the alignment. For each ring and each subunit, the angular distance of its normal vector to all other normal vectors of subunits within the same ring was computed. Subsequently, the distances were averaged (for each NPC separately), and for each subunit, the deviation from the normal vector from the average was computed. The same was done for so-called in-plane vectors, that is, vectors describing the direction from the NPC center to the center of a subunit. The expected/ideal angular distance for the normal vectors is zero, while for the in-plane vectors it is 45°. This analysis was performed only on the rings with at least three subunits that were retained from the initial subtomogram averaging runs. The rings with fewer than three subunits were removed from further processing. The computed deviations were used to identify poorly aligned ring subunits in order to remove them. For CR and SR, all subunits with the normal vector deviation >30° were removed. The deviation of in-plane angles from expected 45° greater than 15° or CR and 10° for SR was used as threshold for additional removal of ring subunits. The threshold values were determined empirically. For CR and SR, the number of subunits left for processing after geometrical cleaning were 31,774 and 35,281, respectively. The geometrical-restrain classification was added

to the publicly available novaSTA package (71). The final subunit cleaning to remove poor-quality subunits was performed on the final average using the constrained cross-correlation (CCC) value, which was computed between each subtomogram and the reference during the last iteration of alignment. Subtomograms with the worst CCC values were subsequently removed in batches of 1000, as long as the resolution improved. The number of subunits or subtomograms contributing toward the final structure of the CR and SR ring were 21,604 and 30,000, respectively.

In contrast to CR and IR, adding additional tilt series followed by geometric cleaning procedure on NR did not vield any significant improvement in comparison to the dataset reported by Kosinski et al. (19). Thus, the original map of the NR was used for the presented analysis. The map was created using steps described by Kosinski et al. (19), and the total number of particles contributing to the final average was 11,112.

Cryo-electron tomography and subtomogram averaging of human NPC in cellulo

Data acquisition was performed on a Titan Krios G2 (for HeLa) or G4 (for HEK) (Thermo Fisher), operating at 300 kV and equipped with Gatan K2 Summit direct electron detector and energy filter as described before (23). In brief, tilt series were acquired in dosefractionation mode at 4k by 4k resolution with a nominal pixel size of 3.37 (HeLa) or 3.45 Å (HEK) using an automated dosesymmetric acquisition scheme (74) starting at a given pre-tilt corresponding to the tilt of the FIB-milled lamellae (typically ±13°). Tilt series were acquired with a tilt increment of 3° and a tilt range interval of -50°/+50°, and a total dose per tomogram of 120 to 150 $e^{-}/Å^{2}$.

Tilt series preprocessing and tomogram reconstruction was performed as described previously (22, 23). Subtomogram averaging was performed as described before (22, 23). In brief, for the HeLa control dataset, 53 NPCs were extracted from 13 tomograms. For the HEK dataset, 30 control and 43 NUP210Δ NPCs were extracted from 8 control and 14 NUP210Δ tomograms, respectively. Whole pores were aligned using bin8 and bin4 subtomograms with imposed eightfold symmetry. Upon convergence, 280, 150, and 222 subunits were extracted from the control HeLa, control HEK. and HEK NUP210∆ datasets, respectively, and the CR, IR, and NR subunits were further refined independently using bin4 subtomograms. The individual ring subunits were refined without splitting the data into independent half sets to a final resolution of <54 Å (NR) and <48 Å (CR and IR) as estimated by Fourier shell correlation (FSC) using the 0.5 criterion for the HEK datasets. For the HeLa dataset, gold-standard criteria were used to calculate the FSC, which resulted in final resolution of 45 Å (CR and IR) and 53 Å (NR).

Structure determination of human NUP155

The gene encoding human NUP155 (UniProt ID: O75694) was synthesized by GeneArt (Life Technologies) and cloned into a modified pFastBac vector, with a His6 tag and an enhanced green fluorescent protein tag followed by an HRV 3C protease site at the N terminus and a Strep tag at the C terminus. The predicted membrane-binding loop (residues 260 to 273) was deleted to improve the protein stability. The resulting construct was expressed in Sf21 insect cells using the Bac-to-Bac baculovirus expression system (Thermo Fisher Scientific). Sf21 cells were cultured in Sf900III medium (Gibco) at 27°C and infected at a density of 1×10^6 to 2×10^6 cells ml⁻¹. After 48 hours of incubation, cells were collected by centrifugation (3000g, 10 min, 27°C), and the pellets were stored at -80°C until purification.

For purification, frozen cell pellet from 100 ml culture was resuspended in 10 ml of buffer containing 20 mM HEPES (pH 7.5), 100 mM NaCl, 1 mM dithiothreitol (DTT), and 0.1 mM phenylmethylsulfonyl fluoride and disrupted by sonication for 5 min using Branson sonifier 250. After removing cell debris by centrifugation (3000g, 10 min, 4°C), the supernatant was mixed with 500 µl of Strep-Tactin Sepharose resin (IBA Lifesciences) and incubated at 4°C for 30 min. The resin was washed with 8 ml of buffer containing 20 mM HEPES (pH 7.5), 100 mM NaCl, and 1 mM DTT, and the bound sample was eluted with the same buffer supplemented with 5 mM biotin. The eluted fractions were concentrated with an Amicon Ultra 0.5 ml centrifugal filter (100 kDa molecular weight cut-off, Millipore), mixed with Turbo-3C protease (Sigma-Aldrich), and incubated at 4°C overnight. The sample was then ultracentrifuged (71,680g, 15 min, 4°C) and loaded onto Superose 6 Increase 3.2/300 equilibrated with 20 mM HEPES (pH 7.5), 100 mM NaCl, and 1 mM DTT. The peak fractions were aliquoted and stored at -80°C until use.

For the preparation of EM grids, the protein concentration was adjusted to 0.4 mg ml⁻¹ in 20 mM HEPES (pH 7.5), 100 mM NaCl, 1 mM DTT, and 0.001% dodecyl maltoside. The diluted sample was then applied onto a freshly glowdischarged UltrAuFoil R0.6/1.0 gold grids (300 mesh, Quantifoil), blotted for 6 s at 4°C in 100% humidity, and plunge-frozen in liquid ethane using Vitrobot Mark IV. Cryo-EM data were collected on a Titan Krios G4 microscope (Thermo Scientific) operated at 300 kV, equipped with a E-CFEG, a Falon 4 direct electron detector (Thermo Scientific), and a Selectris X energy filter (Thermo Scientific) operated with a slit width of 10 eV. Automated data acquisition was performed with the EPU software at a nominal magnification of ×165,000, corresponding to a pixel size of 0.730 Å per pixel. Movies were acquired at a dose rate of 4.95 electrons per pixel per second, and a total dose of $50~{\rm e^-/{\rm A}^2}$, resulting in EER movies consisting of 1407 frames. In total, 6430 movies were acquired with a defocus range of -1.0 to $-2.0~{\rm \mu m}$. Acquired images were first processed in cryoSPARC (75), and selected particles were further processed in RELION-3.1 using csparc2star.py script in UCSF pyem (76) for transfer of particles. To analyze the conformational flexibility, multibody refinement (77) was performed on the consensus map. The details of data processing are summarized in fig. S8.

The model of human NUP155 was manually built in *Coot* (78), using the crystal structure of Nup170, a homolog of NUP155, from *C. thermophilum* (PDB ID: 5HAX) as a starting model. Secondary structure prediction from PSIPRED (79) and multiple sequence alignment were used to facilitate the model building. The model was iteratively refined using phenix.real_space_refine (80). Figures were prepared with UCSF Chimera (81), UCSF ChimeraX (82), and CueMol (http://www.cuemol.org/).

Proximity labeling using BioID

BioID analysis of ALADIN was done as previously described (83). In brief, ALADIN was BirA-tagged and overexpressed in Hek293 Flp-In Trex cells. Quantitative mass spectrometry was done in four biological replicates and in comparison to control cells expressing BirA-tagged NLS-NES-Dendra that resides within the central channel.

Structural modeling of NUPs and NPC subcomplexes

The structures of all individual NUPs and selected subcomplexes were modeled using AlphaFold (26) or downloaded from AlphaFold Database (60). The models of monomeric proteins (NUP155, NUP133, NUP107, NUP93, NUP205, NUP188, NUP160, NUP358, and ELYS) were download from AlphaFold Database (60). To model subcomplexes or their parts around the interfaces (NUP62-NUP54-NUP58, NUP205-NUP93, NUP188-NUP93, NUP155-NUP35, NUP93-NUP35, NDC1-ALADIN, NUP35 homodimer, NUP85-SEH1-NUP43, NUP160-NUP96-SEC13, NUP160-NUP37, NUP133-NUP107, NUP96-NUP107, NUP160-NUP96-NUP85, NUP214-NUP62-NUP88, and NUP88-NUP98), we used the AlphaFold version modified for modeling complexes, available through ColabFold (35), with all parameters set to default except for the max_recycles parameter, which was set to between 12 and 48, depending on the subcomplex. For NUP210, we first built the initial fulllength using RoseTTAfold (27), as AlphaFold did not provide a full-length model fitting well into the EM density map. After fitting the model into the EM maps as a rigid body

(see below), we used AlphaFold to model successive monomeric and homodimeric fragments of NUP210, superposed them onto the fitted RoseTTAfold model, and refined the fits. The quality of the AlphaFold models was first assessed by the scores provided by the authorsthe predicted local distance difference test (pLDDT), which predicts the local accuracy, and predicted aligned error, which assesses the packing between domains and protein chains. In addition, we validated the models by comparing to structures not used for modeling, structures published in the accompanying paper (32), fits to the cryo-ET maps, and previously published biochemical data (figs. S5 to S7, S10, S11, and S14).

Systematic fitting of atomic structures to cryo-ET maps

We used the previously published procedure for systematic fitting (8, 19, 21, 22, 25, 37, 84) to both locate the atomic structures in the cryo-ET maps and validate the AlphaFold models. Before fitting, all the high-resolution structures were filtered to between 10 and 15 Å. The resulting simulated model maps were subsequently fitted into individual ring segments of cryo-ET maps by global fitting as implemented in UCSF Chimera (82) using scripts in Assembline (37). The maps used for fitting excluded nuclear envelope density in order to eliminate the possibility of fits overlapping with the membrane. All fitting runs were performed using 100,000 random initial placements, with the requirement of at least 30 to 60% (depending on the size of the structure) of the simulated model map to be covered by the cryo-ET density envelope defined at a low threshold. For each fitted model, this procedure resulted in ~1000 to 20,000 fits with nonredundant conformations upon clustering. The cross-correlation about the mean (cam score, equivalent to Pearson correlation) score from UCSF Chimera (81) was used as a fitting metric for each atomic structure, similarly to our previously published works. The statistical significance of every fitted model was evaluated as a P value derived from the cam scores. The calculation of P values was performed by first transforming the cross-correlation scores to z-scores (Fisher's z-transform) and centering, from which subsequently two-sided P values were computed using standard deviation derived from an empirical null distribution [based on all obtained nonredundant fits and fitted using fdrtool (85) R-package]. Finally, the P values were corrected for multiple testing with Benjamini-Hochberg procedure (86).

Modeling of the human NPC scaffold

To assemble the models of the entire NPC scaffold based on the constricted and dilated cryo-ET maps, we used our integrative modeling software Assembline (37), which is based

on Integrative Modeling Platform (IMP) (87) version 2.15 and Python Modeling Interface (PMI) (88). First, we built the model of the constricted NPC owing to its higher resolution. The AlphaFold models of NUP domains and subcomplexes already present in our previous human NPC models (19, 21) were placed in the map by superposing them onto the published models. The remaining domains and subcomplexes added in this work (NUP358. NUP35, NUP93 in the outer rings, NDC, ALADIN, and the NUP214 complex) were placed using systematic fitting (as above) and global optimization procedure of Assembline. In addition to using models of subcomplexes as rigid bodies for fitting, several inter-subunit interfaces were restrained by elastic distance network derived from ColabFold models overlapping with and bridging already fitted models. During the refinement, the structures were used as rigid bodies and simultaneously represented at two resolutions: in Cα-only representation and a coarse-grained representation, in which each 10-residue stretch was converted to a bead. The 10-residue bead representation was used for all restraints to increase computational efficiency except for the domain connectivity restraints, for which the Ca-only representation was used. The flexible protein linkers between the domains were added as chains of one-residue beads. The entire structure was optimized using the refinement step of Assembline to optimize the fit to the map, minimize steric clashes, and ensure connectivity of the protein linkers. The scoring function for the refinement comprised the EM fit restraint; clash score (SoftSpherePairScore of IMP); connectivity distance between domains neighboring in sequence; a term preventing overlap of the protein mass with the nuclear envelope; a restraint promoting the membranebinding loops of NUP133, NUP160, and NUP155 to interact with the envelope implemented using MapDistanceTransform of IMP [predicted by similarity to known or predicted ALPS motifs X. laevis and S. cerevisiae homo- $\log (6, 21, 89)$; and elastic network restraints derived from the subcomplexes modeled with AlphaFold/ColabFold. The final atomic structures were generated from the refined models by back-mapping the coarse-grained representation to the original AlphaFold atomic models. The conformation of the linkers was further optimized using Modeller (90) and Isolde (91). The stereochemistry of the final model was optimized using steepest descent minimization in GROMACS (92).

The model of the dilated NPC was built by fitting the asymmetric units of the individual cytoplasmic, inner, and nuclear rings of the constricted NPC model to the dilated cryo-ET maps and refining the fits with Assembline. The refinement procedure was performed as above

To calculate the percentage of the molecular weight of the full NPC and the NPC scaffold covered by the new and the old models, we defined the full NPC as being composed of the following 32 NUPs, with the stoichiometry indicated in the parentheses: NUP160 (32), NUP96 (32), NUP85 (32), SEH1 (32), SEC13 (32), NUP107 (32), NUP133 (32), NUP358 (40), NUP43 (32), ELYS (16), NUP37 (32), NUP188 (16), NUP205 (40), NUP155 (48), NUP93 (56), NUP35 (32), NUP62 (48), NUP54 (32), NUP58 (32), NUP88 (16), NUP214 (16), NUP98 (48), NDC1 (16), NUP210 (64), and ALADIN (16), POM121 (32), TPR (32), NUP153 (32), NUP50 (16), CG1 (8), DDX19 (16), and GLE1 (8). The scaffold NPC was defined as being composed of 25 NUPs: NUP160, NUP96, NUP85, SEH1, SEC13, NUP107, NUP133, NUP358, NUP43, ELYS, NUP37, NUP188, NUP205, NUP155, NUP93, NUP35, NUP62, NUP54, NUP58, NUP88, NUP214, NUP98, NDC1, NUP210, and ALADIN. The stoichiometry for the scaffold was the same as for the full NPC with exception of NUP214 complex for which only one copy was counted, as the second copy is not clearly visible in the EM density. Note that for some nucleoporins, like NUP98 or POM121, the exact stoichiometry is still uncertain. The coiled-coil domains of the peripheral NUPs of the NUP214 complex and the α-solenoid domain of NUP358 were included in the scaffold. The FG regions were excluded. These definitions resulted in the molecular weight of 119 MDa for the full NPC and 76 MDa for the scaffold. The scaffold diameters were described by two distances between the opposite spokes: the membrane-to-membrane distance and the distance between ferredoxin-like domains of NUP54 at the residue 220. Figures were produced using UCSF ChimeraX (82).

Molecular dynamics (MD) simulations

We performed MD simulations of half-toroidal membrane pores in isolation and including the hNPC scaffold. In the following section, we describe the setup of the simulation models, the relevant MD parameters, and the analysis of the MD trajectories.

Membrane model

First, a 30 nm by 30 nm coarse-grained POPC lipid bilayer patch was generated using insane.py (93, 94). The bilayer was placed in a periodic simulation box, solvated on both sides, energy minimized, and simulated for 100 ns using standard MD parameters, as noted below.

Then, half-toroidal membrane pores were constructed with the BUMpy software (93) using this initial flat bilayer as membrane input. The following command line flags were used when running bumpy: -s double_bilayer_ cylinder -z 10 -g l cylinder:10 r cylinder:430 r_junction:120 l_flat:1400 (see bumpy docu-

mentation). The resulting membranes coincided reasonably with the cryo-ET density of the double-membrane pore and allowed us to place the membrane-anchoring motifs of the NPC model into the membrane.

Two carbon nanotube porins (CNTPs) were inserted into the membrane in the corners of the simulation box distant from the NPC (see, e.g., fig. S19A). The CNTPs with a length of 3.6 nm and a diameter of 14.7 nm enable water transfer in and out of the otherwise disconnected luminal volume, as is required for membrane-mechanical equilibration. Without CNTPs, the luminal volume would be effectively fixed and, as a result, changes in the membrane shape during MD simulations without NPC scaffold would induce artifactual membrane buckling. The CNTPs were built according to previous work (93-95). The outermost carbon rings at either CNTP end consisted of polar SNda beads for stable membrane embedding (93). To stiffen the wide CNTPs, the improper dihedral force constant was increased to 1000 kJ mol⁻¹ rad⁻². The CNTP parameters were otherwise set as previously reported (95, 96). The code to generate CNTP models and the parameters for simulations are available at: https://github.com/bio-phys/ cnt-martini (95). The CNTPs were embedded in the flat patch of the NPC membranes away from the NPC. Lipids within 8 Å of the CNTPs or inside their circumference were removed.

NPC scaffold model

The MD simulation model of the NPC included the entire scaffold (see table S4 and fig. S19 for a summary of the hNPC simulation model) except for the disordered FG-NUP C- and N-terminal tails. For simplicity and to limit the system size, we also excluded the NUP210 glycoprotein in the nuclear envelope lumen. Otherwise, the models were complete as described above.

Each protein chain was coarse-grained individually using martinize.py as follows. All chain termini were uncharged and otherwise default protonation states were used. Secondary structure restraints were assigned according to DSSP (97). The tertiary structure of each protein chain was maintained by an elastic network using the recommended default settings with a cutoff $R_{\rm c}$ of 0.9 nm and a force constant k of 500 kJ mol⁻¹ nm⁻². For each protein chain, the ElNeDyn2.2 protein force field was used in conjunction with the Martini 2.2 force field (53, 54). Simulations were performed with the default protein-protein interaction ($\alpha = 1.0$: results shown in the supplementary materials) and with protein-protein interactions scaled relative to protein-solvent interactions with $\alpha = 0.7$ (98) (results shown in the main text) to correct for the effect of reportedly overestimated nonbonded interactions (99). This procedure used the martinize.py script and was wrapped in custom python code to automatically generate the structures for each protein chain with the aforementioned parameters. To enable easier handling of the large number of protein chains, each protein chain was assigned a unique segid. Importantly, with this MD simulation model, all protein-protein interactions between distinct chains could dissociate and new interactions could form in principle, and the structure of linker regions could relax.

All individually coarse-grained protein chains were then merged into one PDB structure file. The resulting coarse-grained NPC scaffold model was centered within the half-toroidal membrane pore model containing the CNTPs described above. Any lipids within 8 Å of any bead of the scaffold proteins in the initial assembly were removed.

Solvation

All systems were solvated with coarse-grained water containing 10% anti-freeze WF particles and Na⁺ ions to neutralize the system using standard GROMACS tools. All systems simulated in this study are listed in table S5.

MD simulations

All molecular dynamics simulations were performed using the GROMACS software package and the coarse-grained Martini force field v2.2 (53, 92, 100). Each system was first steepestdescent energy minimized using a soft-core potential to remove steric clashes in the initial model. The systems were then equilibrated in an NPT ensemble with semisotropic pressure coupling first for 2.5 ns with a 5-fs timestep and then for 100 ns with a 15-fs timestep with position restraints on the protein backbone beads with a force constant of 1000 kJ mol⁻¹ nm⁻², maintaining a temperature of 310 K and pressure of 1 bar using the Berendsen barostat and velocity rescaling thermostat (101, 102). Characteristic coupling times of 12 and 1 ps were used, respectively. During production simulations, the Parrinello-Rahman barostat was used (103).

The Verlet neighbor search algorithm was used to update the neighbor list, with the length and update frequency being automatically determined. Lennard-Jones and Coulomb forces were cut off at 1.1 nm, with the potential shifted to zero using the Verlet-shift potential modifier. A 15-fs timestep was used in all production simulations. Production simulations were performed for ~1.2 µs each.

Membrane tension

To apply lateral tension on the doublemembrane structure, an anisotropic pressure tensor was used with an out-of-plane pressure of $P_{\perp}=2\Delta P/3$ and an in-plane pressure of $P_{\parallel}=p-\Delta P/3$, with p=1 bar. This results in a traceless lateral strain $S=diag(-\Delta P/3,-\Delta P/3,2\Delta P/3)$ where $\Delta P\equiv P_{\perp}-P_{\parallel}$. The resulting tension on the double-membrane system is $\sigma=(P_{\perp}-P_{\parallel})L_z=\Delta PL_z$ with L_z the box height. To allow for gradual equilibration under tension, ΔP was increased in steps of 1 bar until reaching the target value (see table S1).

Analysis of MD simulations

Images and movies were generated using VMD (104) and time series were analyzed using the MDAnalysis library (105). To monitor conformational changes, we calculated the root-mean-square distance (RMSD) from the starting structure using the qcprot RMSD alignment algorithm implemented in MDAnalysis (105). The RMSD was calculated every 1.5 ns for the backbone (BB) beads with respect to the rigid-body aligned initial structure. In addition to the individual protein chains, we analyzed in this way the β -propeller present in the three nucleoporins NUP133 (residues 1 to 480), NUP155 (residues 1 to 500), and NUP160 (residues 1 to 500); as well as the respective alpha solenoid domain NUP133 (residues 500 to end), and NUP155, and NUP160 (residues 507 to end); and each of the eight spokes as a whole. In the RMSD analysis, averages and standard deviations were calculated across the eight spokes or across equivalent protein copies in the NPC scaffold, respectively.

During the MD simulations, the diameter of the NPC membrane pore was determined by least-square fitting the center and radius of a circle in the xy-plane to the membrane center (C4A and C4B lipid beads). The fit was performed at the narrowest region of the half-toroidal membrane pore.

Possible limitations

We note that the time scale currently accessible to MD simulations is too short to fully recapitulate the complete NPC dilation and constriction processes, including the largescale NPC structural rearrangements. We also note that the elastic network on proteins of the Martini model restricts internal conformational changes, which might be required for larger-scale NPC dilation. The coarse-grained interaction model may also weaken some protein-protein interactions and strengthen others. Finally, we expect that the missing FG mesh in the MD model contributes to the compaction of the NPC scaffold seen in the MD simulations, acting on top of the mechanical tension in the widened double-membrane pore (supplementary text).

REFERENCES AND NOTES

- A. Ibarra, M. W. Hetzer, Nuclear pore proteins and the control of genome functions. *Genes Dev.* 29, 337–349 (2015). doi: 10.1101/gad.256495.114; pmid: 25691464
- M. Raices, M. A. D'Angelo, Nuclear pore complexes and regulation of gene expression. Curr. Opin. Cell Biol. 46,

- 26–32 (2017). doi: 10.1016/j.ceb.2016.12.006; pmid: 28088069
- C. Strambio-De-Castillia, M. Niepel, M. P. Rout, The nuclear pore complex: Bridging nuclear transport and gene regulation. *Nat. Rev. Mol. Cell Biol.* 11, 490–501 (2010). doi: 10.1038/nrm2928; pmid: 20571586
- P. De Magistris, W. Antonin, The dynamic nature of the nuclear envelope. *Curr. Biol.* 28, R487–R497 (2018). doi: 10.1016/j.cub.2018.01.073; pmid: 29689232
- B. Hampoelz, A. Andres-Pons, P. Kastritis, M. Beck, Structure and assembly of the nuclear pore complex. *Annu. Rev. Biophys.* 48, 515–536 (2019). doi: 10.1146/annurev-biophys-052118-115308; pmid: 30943044
- D. H. Lin, A. Hoelz, The structure of the nuclear pore complex (an update). *Annu. Rev. Biochem.* 88, 725–783 (2019). doi: 10.1146/annurev-biochem-062917-011901; pmid: 30883195
- S. Siniossoglou et al., Structure and assembly of the Nup84p complex. J. Cell Biol. 149, 41–54 (2000). doi: 10.1083/ jcb.149.1.41; pmid: 10747086
- K. H. Bui et al., Integrated structural analysis of the human nuclear pore complex scaffold. Cell 155, 1233–1243 (2013). doi: 10.1016/j.cell.2013.10.055; pmid: 24315095
- M. Beck, E. Hurt, The nuclear pore complex: Understanding its function through structural insight. *Nat. Rev. Mol. Cell Biol.* 18, 73–89 (2017). doi: 10.1038/nrm.2016.147; pmid: 27999437
- J. Fischer, R. Teimer, S. Amlacher, R. Kunze, E. Hurt, Linker Nups connect the nuclear pore complex inner ring with the outer ring and transport channel. *Nat. Struct. Mol. Biol.* 22, 774–781 (2015). doi: 10.1038/nsmb.3084; pmid: 26344569
- D. H. Lin et al., Architecture of the symmetric core of the nuclear pore. Science 352, aaf1015 (2016). doi: 10.1126/ science.aaf1015; pmid: 27081075
- S. J. Kim et al., Integrative structure and functional anatomy of a nuclear pore complex. Nature 555, 475–482 (2018). doi: 10.1038/nature26003; pmid: 29539637
- T. Stuwe et al., Architecture of the fungal nuclear pore inner ring complex. Science 350, 56–64 (2015). doi: 10.1126/ science.aac9176; pmid: 26316600
- S. G. Brohawn, T. U. Schwartz, Molecular architecture of the Nup84-Nup145C-Sec13 edge element in the nuclear pore complex lattice. *Nat. Struct. Mol. Biol.* 16, 1173–1177 (2009). doi: 10.1038/nsmb.1713; pmid: 19855394
- S. O. Obado et al., Interactome mapping reveals the evolutionary history of the nuclear pore complex. PLOS Biol. 14, e1002365 (2016). doi: 10.1371/journal.pbio.1002365; pmid: 26891179
- A. G. Floch, B. Palancade, V. Doye, Fifty years of nuclear pores and nucleocytoplasmic transport studies: Multiple tools revealing complex rules. *Methods Cell Biol.* 122, 1-40 (2014). doi: 10.1016/B978-0-12-417160-2.00001-1; pmid: 24857723
- D. Görlich, U. Kutay, Transport between the cell nucleus and the cytoplasm. Annu. Rev. Cell Dev. Biol. 15, 607–660 (1999). doi: 10.1146/annurev.cellbio.15.1.607; pmid: 10611974
- E. A. Lemke, The multiple faces of disordered nucleoporins.
 J. Mol. Biol. 428, 2011–2024 (2016). doi: 10.1016/ j.jmb.2016.01.002; pmid: 26791761
- J. Kosinski et al., Molecular architecture of the inner ring scaffold of the human nuclear pore complex. Science 352, 363–365 (2016). doi: 10.1126/science.aaf0643; pmid: 27081072
- A. P. Schuller et al., The cellular environment shapes the nuclear pore complex architecture. Nature 598, 667–671 (2021). doi: 10.1038/s41586-021-03985-3; pmid: 34646014
- A. von Appen et al., In situ structural analysis of the human nuclear pore complex. Nature 526, 140–143 (2015). doi: 10.1038/nature15381; pmid: 26416747
- M. Allegretti et al., In-cell architecture of the nuclear pore and snapshots of its turnover. Nature 586, 796–800 (2020). doi: 10.1038/s41586-020-2670-5; pmid: 32879490
- C. E. Zimmerli et al., Nuclear pores dilate and constrict in cellulo. Science 374, eabd9776 (2021). doi: 10.1126/science. abd9776; pmid: 34762489
- M. Beck, S. Mosalaganti, J. Kosinski, From the resolution revolution to evolution: Structural insights into the evolutionary relationships between vesicle coats and the nuclear pore. *Curr. Opin. Struct. Biol.* 52, 32–40 (2018). doi: 10.1016/j.sbi.2018.07.012; pmid: 30103204

- S. Mosalaganti et al., In situ architecture of the algal nuclear pore complex. Nat. Commun. 9, 2361 (2018). doi: 10.1038/ s41467-018-04739-y; pmid: 29915221
- J. Jumper et al., Highly accurate protein structure prediction with AlphaFold. Nature 596, 583–589 (2021). doi: 10.1038/ s41586-021-03819-2; pmid: 34265844
- M. Baek et al., Accurate prediction of protein structures and interactions using a three-track neural network. Science 373, 871–876 (2021). doi: 10.1126/science.abj8754; pmid: 34282049
- T. Maimon, N. Elad, I. Dahan, O. Medalia, The human nuclear pore complex as revealed by cryo-electron tomography. Structure 20, 998–1006 (2012). doi: 10.1016/ j.str.2012.03.025; pmid: 22632834
- J. Mahamid et al., Visualizing the molecular sociology at the HeLa cell nuclear periphery. Science 351, 969–972 (2016). doi: 10.1126/science.aad8857; pmid: 26917770
- V. Zila et al., Cone-shaped HIV-1 capsids are transported through intact nuclear pores. Cell 184, 1032–1046.e18 (2021). doi: 10.1016/j.cell.2021.01.025; pmid: 33571428
- C. J. Bley et al., Architecture of the cytoplasmic face of the nuclear pore. Science 376, eabm9129 (2022). doi: 10.1126/science.abm9129
- S. Petrovic et al., Architecture of the linker-scaffold in the nuclear pore. Science 376, eabm9798 (2022). doi: 10.1126/science.abm9798
- G. Huang et al., Structure of the cytoplasmic ring of the Xenopus laevis nuclear pore complex by cryo-electron microscopy single particle analysis. Cell Res. 30, 520–531 (2020). doi: 10.1038/s41422-020-0319-4; pmid: 32376910
- R. Evans et al., Protein complex prediction with AlphaFold-Multimer. bioRxiv 2021.10.04.463034 [Preprint] (2021). https://doi.org/10.1101/2021.10.04.463034.
- M. Mirdita et al., ColabFold Making protein folding accessible to all. bioRxiv 2021.08.15.456425 [Preprint] (2021). https://doi.org/10.1101/2021.08.15.456425.
- I. R. Humphreys et al., Computed structures of core eukaryotic protein complexes. Science 374, eabm4805 (2021). doi: 10.1126/science.abm4805; pmid: 34762488
- V. Rantos, K. Karius, J. Kosinski, Integrative structural modeling of macromolecular complexes using Assembline. Nat. Protoc. 17, 152–176 (2022). doi: 10.1038/s41596-021-00640-z; pmid: 34845384
- N. Schrader et al., Structural basis of the nic96 subcomplex organization in the nuclear pore channel. Mol. Cell 29, 46–55 (2008). doi: 10.1016/j.molcel.2007.10.022; pmid: 18206968
- B. Vollmer et al., Dimerization and direct membrane interaction of Nup53 contribute to nuclear pore complex assembly. EMBO J. 31, 4072–4084 (2012). doi: 10.1038/ emboj.2012.256; pmid: 22960634
- J. Mansfeld et al., The conserved transmembrane nucleoporin NDC1 is required for nuclear pore complex assembly in vertebrate cells. Mol. Cell 22, 93–103 (2006). doi: 10.1016/ j.molcel.2006.02.015; pmid: 16600873
- Y. Yamazumi et al., The transmembrane nucleoporin NDC1 is required for targeting of ALADIN to nuclear pore complexes. Biochem. Biophys. Res. Commun. 389, 100–104 (2009). doi: 10.1016/j.bbrc.2009.08.096; pmid: 19703420
- B. Kind, K. Koehler, M. Lorenz, A. Huebner, The nuclear pore complex protein ALADIN is anchored via NDC1 but not via POMI21 and GP210 in the nuclear envelope. *Biochem. Biophys. Res. Commun.* 390, 205–210 (2009). doi: 10.1016/jbbr.2009.09.080; pmid: 19782045
- A. Ori et al., Cell type-specific nuclear pores: A case in point for context-dependent stoichiometry of molecular machines. Mol. Syst. Biol. 9, 648 (2013). doi: 10.1038/msb.2013.4; pmid: 23511206
- N. Eisenhardt, J. Redolfi, W. Antonin, Interaction of Nup53 with Ndc1 and Nup155 is required for nuclear pore complex assembly. J. Cell Sci. 127, 908–921 (2014). pmid: 24363447
- D. H. Lin et al., Structural and functional analysis of mRNA export regulation by the nuclear pore complex. Nat. Commun. 9, 2319 (2018). doi: 10.1038/s41467-018-04459-3; pmid: 29899397
- J. M. Cronshaw, M. J. Matunis, The nuclear pore complex protein ALADIN is mislocalized in triple A syndrome. Proc. Natl. Acad. Sci. U.S.A. 100, 5823–5827 (2003). doi: 10.1073/pnas.1031047100; pmid: 12730363
- A. Huebner et al., The triple A syndrome is due to mutations in ALADIN, a novel member of the nuclear pore complex. Endocr. Res. 30, 891–899 (2004). doi: 10.1081/ERC-200044138; pmid: 15666842

- A.-R. Cho et al., Tissue-specific expression and subcellular localization of ALADIN, the absence of which causes human triple A syndrome. Exp. Mol. Med. 41, 381–386 (2009). doi: 10.3858/emm.2009.41.6.043; pmid: 19322026
- P. Upla et al., Molecular architecture of the major membrane ring component of the nuclear pore complex. Structure 25, 434–445 (2017). doi: 10.1016/j.str.2017.01.006; pmid: 28162953
- Y. Zhang et al., Molecular architecture of the luminal ring of the Xenopus laevis nuclear pore complex. Cell Res. 30, 532–540 (2020). doi: 10.1038/s41422-020-0320-y; pmid: 32367042
- E. Onischenko, L. H. Stanton, A. S. Madrid, T. Kieselbach, K. Weis, Role of the Ndc1 interaction network in yeast nuclear pore complex assembly and maintenance. *J. Cell Biol.* 185, 475–491 (2009). doi: 10.1083/jcb.200810030; pmid: 19414609
- D. Devos et al., Components of coated vesicles and nuclear pore complexes share a common molecular architecture. PLOS Biol. 2, e380 (2004). doi: 10.1371/journal. pbio.0020380; pmid: 15523559
- S. J. Marrink, H. J. Risselada, S. Yefimov, D. P. Tieleman, A. H. de Vries, The MARTINI force field: Coarse grained model for biomolecular simulations. J. Phys. Chem. B 111, 7812–7824 (2007). doi: 10.1021/jp071097f; pmid: 17569554
- X. Periole, M. Cavalli, S.-J. Marrink, M. A. Ceruso, Combining an elastic network with a coarse-grained molecular force field: Structure, dynamics, and intermolecular recognition. *J. Chem. Theory Comput.* 5, 2531–2543 (2009). doi: 10.1021/ ct9002114; pmid: 26616630
- J. G. Gall, Octagonal nuclear pores. J. Cell Biol. 32, 391–399 (1967). doi: 10.1083/jcb.32.2.391; pmid: 10976230
- C. Wolf, M. R. K. Mofrad, On the octagonal structure of the nuclear pore complex: Insights from coarse-grained models. *Biophys. J.* 95, 2073–2085 (2008). doi: 10.1529/ biophysj.108.130336; pmld: 18487299
- M. Seidel et al., Co-translational assembly orchestrates competing biogenesis pathways. Nat. Commun. 13, 1224 (2022). doi: 10.1038/s41467-022-28878-5; pmid: 35264577
- J. P. Stafstrom, L. A. Staehelin, Dynamics of the nuclear envelope and of nuclear pore complexes during mitosis in the Drosophila embryo. Eur. J. Cell Biol. 34, 179–189 (1984). pmid: 6428889
- S. Otsuka et al., Postmitotic nuclear pore assembly proceeds by radial dilation of small membrane openings. Nat. Struct. Mol. Biol. 25, 21–28 (2018). doi: 10.1038/s41594-017-0001-9; pmid: 29323269
- K. Tunyasuvunakool et al., Highly accurate protein structure prediction for the human proteome. Nature 596, 590–596 (2021). doi: 10.1038/s41586-021-03828-1; pmid: 34293799
- M. Akdel et al., A structural biology community assessment of AlphaFold 2 applications. bioRxiv 2021.09.26.461876 [Preprint] (2021). https://doi.org/10.1101/ 2021.09.26.461876
- G. Masrati et al., Integrative structural biology in the era of accurate structure prediction. J. Mol. Biol. 433, 167127 (2021). doi: 10.1016/j.jmb.2021.167127; pmid: 34224746
- J. Pereira et al., High-accuracy protein structure prediction in CASP14. Proteins 89, 1687–1699 (2021). doi: 10.1002/ prot.26171; pmid: 34218458
- V. Ruiz-Serra et al., Assessing the accuracy of contact and distance predictions in CASP14. Proteins 89, 1888–1900 (2021). doi: 10.1002/prot.26248; pmid: 34595772
- J. Jumper et al., Applying and improving AlphaFold at CASP14. Proteins 89, 1711–1721 (2021). doi: 10.1002/ prot.26257; pmid: 34599769
- P. Bryant, G. Pozzati, A. Elofsson, Improved prediction of protein-protein interactions using AlphaFold2. *Nat. Commun.* 13, 1265 (2022). doi: 10.1038/s41467-022-28865-w; pmid: 35273146
- K. Buczak, "Spatial proteomics: from tissue organization to protein function," thesis, Universität Heidelberg (2019). doi: 10.11588/HEIDOK.00025909
- A. Rohou, N. Grigorieff, CTFFIND4: Fast and accurate defocus estimation from electron micrographs. *J. Struct. Biol.* 192, 216–221 (2015). doi: 10.1016/j.jsb.2015.08.008; pmid: 26278980
- D. N. Mastronarde, S. R. Held, Automated tilt series alignment and tomographic reconstruction in IMOD. J. Struct. Biol. 197, 102–113 (2017). doi: 10.1016/j.jsb.2016.07.011; pmid: 27444399
- B. Turoňová, F. K. M. Schur, W. Wan, J. A. G. Briggs, Efficient 3D-CTF correction for cryo-electron tomography using

- NovaCTF improves subtomogram averaging resolution to 3.4Å. *J. Struct. Biol.* **199**, 187–195 (2017). doi: 10.1016/j.jsb.2017.07.007; pmid: 28743638
- B. Turonova, turonova/novaSTA: Advanced particle analysis, version 1.1, Zenodo (2022): https://doi.org/10.5281/ zenodo.5921012.doi: 10.5281/zenodo.5921012
- D. Castaño-Díez, M. Kudryashev, M. Arheit, H. Stahlberg, Dynamo: A flexible, user-friendly development tool for subtomogram averaging of cryo-EM data in high-performance computing environments. J. Struct. Biol. 178, 139–151 (2012). doi: 10.1016/j.jsb.2011.12.017; pmid: 22245546
- S. H. W. Scheres, RELION: Implementation of a Bayesian approach to cryo-EM structure determination. J. Struct. Biol. 180, 519–530 (2012). doi: 10.1016/j.jsb.2012.09.006; pmid: 23000701
- W. J. H. Hagen, W. Wan, J. A. G. Briggs. Implementation of a cryoelectron tomography tilt-scheme optimized for high resolution subtomogram averaging. J. Struct. Biol. 197, 191–198 (2017). doi: 10.1016/j.jsb.2016.06.007; pmid: 27313000
- A. Punjani, J. L. Rubinstein, D. J. Fleet, M. A. Brubaker, cryoSPARC: Algorithms for rapid unsupervised cryo-EM structure determination. *Nat. Methods* 14, 290–296 (2017). doi: 10.1038/nmeth.4169; pmid: 28165473
- D. Asarnow, E. Palovcak, Y. Cheng, asarnow/pyem: UCSF pyem v0.5, Zenodo (2019); https://doi.org/10.5281/ zenodo.3576630.
- T. Nakane, D. Kimanius, E. Lindahl, S. H. H. W. Scheres, Characterisation of molecular motions in cryo-EM single-particle data by multi-body refinement in RELION. eLife 7, e36861 (2018). doi: 10.7554/eLife.36861; pmid: 29856314
- P. Emsley, B. Lohkamp, W. G. Scott, K. Cowtan, Features and development of Coot. Acta Crystallogr. D Biol. Crystallogr. 66, 486–501 (2010). doi: 10.1107/S0907444910007493; pmid: 20383002
- L. J. McGuffin, K. Bryson, D. T. Jones, The PSIPRED protein structure prediction server. *Bioinformatics* 16, 404–405 (2000). doi: 10.1093/bioinformatics/16.4.404; pmid: 10869041
- P. V. Afonine et al., Real-space refinement in PHENIX for cryo-EM and crystallography. Acta Crystallogr. D Struct. Biol. 74, 531–544 (2018). doi: 10.1107/S2059798318006551; pmid: 29872004
- E. F. Pettersen et al., UCSF Chimera—A visualization system for exploratory research and analysis.
 J. Comput. Chem. 25, 1605–1612 (2004). doi: 10.1002/jcc.20084; pmid: 15264254
- T. D. Goddard et al., UCSF ChimeraX: Meeting modern challenges in visualization and analysis. Protein Sci. 27, 14–25 (2018). doi: 10.1002/pro.3235; pmid: 28710774
- M.-T. Mackmull et al., Landscape of nuclear transport receptor cargo specificity. Mol. Syst. Biol. 13, 962 (2017). doi: 10.15252/msb.20177608; pmid: 29254951
- M. I. Dauden et al., Architecture of the yeast Elongator complex. EMBO Rep. 18, 264–279 (2017). doi: 10.15252/ embr.201643353; pmid: 27974378
- K. Strimmer, fdrtool: A versatile R package for estimating local and tail area-based false discovery rates. *Bioinformatics* 24, 1461–1462 (2008). doi: 10.1093/bioinformatics/btn209; pmid: 18441000
- Y. Benjamini, Y. Hochberg, Controlling the false discovery rate: A practical and powerful approach to multiple testing. J. R. Stat. Soc. B 57, 289–300 (1995). doi: 10.1111/j.2517-6161.1995.tb02031.x
- B. Webb et al., Integrative structure modeling with the Integrative Modeling Platform. Protein Sci. 27, 245–258 (2018). doi: 10.1002/pro.3311; pmid: 28960548
- D. Saltzberg et al., Modeling biological complexes using Integrative Modeling Platform. Methods Mol. Biol. 2022, 353–377 (2019). doi: 10.1007/978-1-4939-9608-7_15; pmid: 31396911
- B. Vollmer et al., Nup153 recruits the Nup107-160 complex to the inner nuclear membrane for interphasic nuclear pore complex assembly. Dev. Cell 33, 717-728 (2015). doi: 10.1016/j.devcel.2015.04.027; pmid: 26051542
- B. Webb, A. Sali, Comparative protein structure modeling using MODELLER. Curr. Protoc. Bioinformatics 54, 5.6.1–5.6.37 (2016). doi: 10.1002/cpbi.3; pmid: 27322406
- T. I. Croll, ISOLDE: A physically realistic environment for model building into low-resolution electron-density maps. Acta Crystallogr. D Struct. Biol. 74, 519–530 (2018). doi: 10.1107/S2059798318002425; pmid: 29872003

- M. J. Abraham et al., GROMACS: High performance molecular simulations through multi-level parallelism from laptops to supercomputers. SoftwareX 1–2, 19–25 (2015). doi: 10.1016/ isoftx.2015.06.001
- K. J. Boyd, E. R. May, BUMPy: A model-independent tool for constructing lipid bilayers of varying curvature and composition. J. Chem. Theory Comput. 14, 6642–6652 (2018). doi: 10.1021/acs.jctc.8b00765; pmid: 30431272
- T. A. Wassenaar, H. I. Ingólfsson, R. A. Böckmann, D. P. Tieleman, S. J. Marrink, Computational Lipidomics with insane: A Versatile tool for generating custom membranes for molecular simulations. J. Chem. Theory Comput. 11, 2144–2155 (2015). doi: 10.1021/acs.jctc.5b00209; pmid: 26574417
- M. Vögele, J. Köfinger, G. Hummer, Molecular dynamics simulations of carbon nanotube porins in lipid bilayers. Faraday Discuss. 209, 341–358 (2018). doi: 10.1039/ C8FD00011E; pmid: 29974904
- R. M. Bhaskara, S. M. Linker, M. Vögele, J. Köfinger, G. Hummer, Carbon nanotubes mediate fusion of lipid vesicles. ACS Nano 11, 1273–1280 (2017). doi: 10.1021/ acsnano.6b05434; pmid: 28103440
- W. Kabsch, C. Sander, Dictionary of protein secondary structure: Pattern recognition of hydrogen-bonded and geometrical features. *Biopolymers* 22, 2577–2637 (1983). doi: 10.1002/bip.360221211; pmid: 6667333
- Z. Benayad, S. von Bülow, L. S. Stelzl, G. Hummer, Simulation of FUS protein condensates with an adapted coarse-grained model. J. Chem. Theory Comput. 17, 525–537 (2021). doi: 10.1021/acs.jctc.0c01064; pmid: 33307683
- M. Javanainen, H. Martinez-Seara, I. Vattulainen, Excessive aggregation of membrane proteins in the Martini model. PLOS ONE 12, e0187936 (2017). doi: 10.1371/journal. pone.0187936; pmid: 29131844
- L. Monticelli et al., The MARTINI coarse-grained force field: Extension to Proteins. J. Chem. Theory Comput. 4, 819–834 (2008). doi: 10.1021/ct700324x; pmid: 26621095
- İ. J. Ć. Berendsen, J. P. M. Postma, W. F. van Gunsteren, A. DiNola, J. R. Haak, Molecular dynamics with coupling to an external bath. *J. Chem. Phys.* 81, 3684–3690 (1984). doi: 10.1063/1.448118
- G. Bussi, D. Donadio, M. Parrinello, Canonical sampling through velocity rescaling. *J. Chem. Phys.* 126, 014101 (2007). doi: 10.1063/1.2408420; pmid: 17212484
- M. Parrinello, A. Rahman, Polymorphic transitions in single crystals: A new molecular dynamics method. *J. Appl. Phys.* 52, 7182–7190 (1981). doi: 10.1063/1.328693
- W. Humphrey, A. Dalke, K. Schulten, VMD: Visual molecular dynamics. J. Mol. Graph. 14, 33–38, 27–28 (1996). doi: 10.1016/0263-7855(96)00018-5; pmid: 8744570
- N. Michaud-Agrawal, E. J. Denning, T. B. Woolf,
 O. Beckstein, MDAnalysis: A toolkit for the analysis of molecular dynamics simulations. J. Comput. Chem. 32, 2319–2327 (2011). doi: 10.1002/jcc.21787; pmid: 21500218

ACKNOWLEDGMENTS

We acknowledge support from the Electron Microscopy Core Facility (EMCF) and IT services of European Molecular Biology Laboratory (EMBL) Heidelberg. We thank S. Welsch at the Central Electron Microscopy Facility of the Max Planck Institute of Biophysics for technical expertise. We thank T. Hoffman and R. Alves for help with the AlphaFold installation. Funding: M.B. acknowledges funding by EMBL, the Max Planck Society, and the European Research Council (ComplexAssembly 724349), J.K. acknowledges funding from the Federal Ministry of Education and Research of Germany (FKZ 031L0100). The work by M.S. and G.H. on computer simulations was supported by the Max Planck Society, M.S. was supported by the EMBL Interdisciplinary Postdoc Programme under Marie Curie COFUND actions, M.S. and G.H. were supported by the Landes-Offensive zur Entwicklung Wissenschaftlich-ökonomischer Exzellenz (LOEWE) DynaMem program of the State of Hessen. Author contributions: S.M. prepared the samples and collected and analyzed the HeLa envelope data. S.M., W.J.H.H., and E.M. collected the HeLa envelope and Hel a in cellulo data, S.M. and B.T. performed the cryo-ET analysis. C.E.Z. prepared, collected, and analyzed the HEK control and NUP210∆ data. R.T. determined the structure of human NUP155. M.-T.M. performed the BioID experiments. F.H.S and K.B. prepared the HEK NUP210∆ cell line. A.O.-K. performed modeling and prepared figures. M.S. performed the MD simulations, G.H. performed the membrane elastic theory analysis. J.K. and A.O.-K. prepared software. S.M., G.H., J.K., and M.B.

conceptualized the study, supervised the project, and wrote the manuscript. CRediT roles: Conceptualization: S.M., A.O.-K., G.H., J.K., and M.B. Methodology: S.M., A.O.-K., B.T., M.S., and J.K. Investigation: S.M., A.O.-K., M.S., R.T., B.T., C.E.Z., K.B., F.H.S., E.M., M.-T.M., W.H., G.H., J.K., and M.B. Visualization: S.M., A.O.-K., M.S., R.T., C.E.Z., M.-T.M., and J.K. Funding acquisition: M.B. Project administration: G.H., J.K., and M.B. Supervision: S.M., G.H., J.K., and M.B. Writing - original draft: S.M., M.S., G.H., M.B., and J.K. Writing - review & editing: S.M., A.O.-K., M.S., G.H., M.B., and J.K. Competing interests: The authors declare that they have no competing interests. Data and materials availability: EM maps associated with the manuscript have been

deposited in the Electron Microscopy Data Bank (EMDB) under accession codes EMD-14243, -14321, -14322, -14325, -14326, -14327, -14328, and -14330. The models have been deposited into the Protein Data Bank (PDB) under accession codes 7R1Y, 7R5K, and 7R5J. The predicted local quality scores (pLDDT) have been reported in the B-factor property of the deposited models. Software code for subtomogram averaging and geometric cleaning is available at Zenodo (71). License information: Copyright © 2022 the authors, some rights reserved; exclusive licensee American Association for the Advancement of Science. No claim to original US government works. https://www.science.org/about/ science-licenses-journal-article-reuse

science.org/doi/10.1126/science.abm9506 Supplementary Text Figs. S1 to S29 Tables S1 to S6 References (106-129) MDAR Reproducibility Checklist

View/request a protocol for this paper from Bio-protocol.

Submitted 24 October 2021; accepted 22 April 2022 10.1126/science.abm9506